DESIGN AND ANALYSIS OF METAMATERIAL BASED BIOSENSOR TO DETERMINE BLOOD GLUCOSE CONCENTRATION

MIR MD. AMINUZZAMAN (SN. 0419160005)

A Thesis Submitted in Partial Fulfillment of the Requirements for the Degree of Master of Science in Electrical, Electronic and Communication Engineering

DEPARTMENT OF ELECTRICAL, ELECTRONIC AND COMMUNICATION ENGINEERING
MILITARY INSTITUTE OF SCIENCE AND TECHNOLOGY
DHAKA, BANGLADESH

JANUARY 2024

DESIGN AND ANALYSIS OF METAMATERIAL BASED BIOSENSOR TO DETERMINE BLOOD GLUCOSE CONCENTRATION

M.Sc. Engineering Thesis

By

MIR MD. AMINUZZAMAN (SN. 0419160005)

Approved as to style and content by the Board of Examination on 21 January 2024:

_____ Dr. Md. Hossam-E-Haider Professor Dept of EECE, MIST	Chairman (Supervisor) Board of Examination
_____ Dr. Satya Prasad Majumder Professor Dept of EEE, BUET	Member (External) Board of Examination
_____ Wg Cdr Toyobur Rahman, PhD Instructor Class A Dept of EECE, MIST	Member (Internal) Board of Examination
_____ Lt Col Md Aminul Islam, PhD Instructor Class A Dept of EECE, MIST	Member (Internal) Board of Examination
_____ Brig Gen Md Rezaul Awal Head Dept of EECE, MIST	Member (Ex-officio) Board of Examination

Department of EECE, MIST, Dhaka

DESIGN AND ANALYSIS OF METAMATERIAL BASED BIOSENSOR TO DETERMINE BLOOD GLUCOSE CONCENTRATION

DECLARATION

I hereby declare that the study reported in this thesis entitled as above has been composed solely by me and it has not been submitted, in whole or in part, in any previous application for any degree. Further I certify that the intellectual content of this thesis is the product of my own work and that all the assistance received in preparing this thesis and sources have been acknowledged or cited in the reference Section.

_____

Mir Md. Aminuzzaman

Department of EECE, MIST, Dhaka

ABSTRACT

Design and Analysis of Metamaterial Based Biosensor to Determine Blood Glucose Concentration

A biosensor utilizing metamaterials for the purpose of detecting blood glucose concentrations is designed and simulated in this study. The proposed sensor consists of a microstrip patch antenna designed on a Rogers RT5880 substrate. A circular-shaped complementary split ring resonator (CSRR) cell is integrated onto the patch of the antenna which acts as a crucial component for the glucose sensing. An investigation is conducted to determine the dimensions of the CSRR, including the number of cells, the radius of the outer and inner rings, and the location of the structure. Various shapes of CSRR, namely circular, square, and hexagonal shapes are explored in order to determine the most optimal configuration for the CSRR. The sensing zone of the sensor is determined based on the analysis of the electric field and surface current. An investigation of the characteristics of the CSRR is performed to illustrate its significance in the field of glucose detection. The sensor is analyzed in order to ascertain the concentration of glucose ranging from 50 mg/dL to 300 mg/dL in both aqueous solutions as well as a human finger model. The sensing parameter is amplitude of reflection coefficient, which exhibits variation in response to alterations in the dielectric characteristics of the sample being tested. The Debye and Cole-Cole relaxation model is employed to estimate the dielectric properties of aqueous and blood glucose solutions respectively. The glucose level is determined through the utilization of a linear regression model that describes the correlation between the magnitude of the reflection coefficient of the sensor and the concentration of glucose. The effects of varying the thickness of different finger tissues are examined. The sensor demonstrates a notable sensitivity of 1.792 dB per ($mgdL^{-1}$) and is capable of determining glucose levels with a good accuracy, as validated through the application of mean absolute relative difference (MARD) and Clarke error grid analysis. The maximum 1-g specific absorption rate (SAR) of the sensor is obtained as 0.519 W/kg which ensures the RF safety of the device. This sensor exhibits enhanced performance compared to some state-of-the-art glucose sensors.

সারসংক্ষেপ

Design and Analysis of Metamaterial Based Biosensor to Determine Blood Glucose Concentration

অত্র প্রবন্ধে রক্তে গ্লুকোজের মাত্রা নির্ণয়ের জন্য মেটাম্যাটেরিয়াল ব্যবহার করে একটি বায়োসেন্সর ডিজাইন ও সিমুলেশন সম্পাদন করা হয়েছে। প্রস্তাবিত সেন্সরে রজার্স আরটি৫৮৮০ সাবস্ট্রেটে ডিজাইন করা একটি মাইক্রোস্টিপ প্যাচ এন্টেনা রয়েছে। এন্টেনার প্যাচ অংশে একটি বৃত্তাকৃতির কমপ্লিমেন্টারি স্প্লিট রিং রেজোনেটর (CSRR) সেল ব্যবহৃত হয়েছে যা গ্লুকোজ সেন্সিংয়ের জন্য একটি গুরুত্বপূর্ণ উপাদান হিসেবে কাজ করে। CSRR এর বিভিন্ন মাপ যেমন সেল এর সংখ্যা, বাইরের ও ভিতরের রিং এর ব্যাসার্ধ এবং কাঠামোর অবস্থান নির্ণয়ের জন্য একটি বিশ্লেষণ সম্পাদিত হয়েছে। CSRR এর সর্বোত্তম আকৃতি নির্ধারণের বিভিন্ন আকার যেমন বৃত্তাকার, বর্গাকার, ষড়ভুজ আকার পরীক্ষা করা হয়েছে। সেন্সরের তড়িৎক্ষেত্র ও পৃষ্ঠদেশের বিদ্যুৎ এর উপর অনুসন্ধান চালিয়ে এর সেন্সিং জোন নির্ধারণ করা হয়েছে। CSRR এর বৈশিষ্ট্য পর্যালোচনা করে গ্লুকোজের মাত্রা নির্ধারণে এর তাৎপর্য নিয়ে আলোচনা করা হয়েছে। সেন্সরটি ব্যবহার করে ৫০ মিলিগ্রাম প্রতি ডেসিলিটার হতে ৩০০ মিলিগ্রাম প্রতি ডেসিলিটার সীমার মধ্যে জলীয় দ্রবণ ও মানব আঙ্গুল মডেল উভয়টিতেই গ্লুকোজের মাত্রা নির্ণয়ের জন্য বিশ্লেষণ সম্পাদন করা হয়েছে। সেন্সিং প্যারামিটার হিসেবে নির্ধারিত হয়েছে প্রতিফলন সহগের মান, যা নমুনার ডাইইলেকট্রিক বৈশিষ্ট্যের পরিবর্তনের সাথে পরিবর্তিত হয়। ডেবঈ ও কোল-কোল মডেল ব্যবহৃত হয়েছে যথাক্রমে জলীয় দ্রবণ ও রক্তে গ্লুকোজের ডাইইলেকট্রিক বৈশিষ্ট্য নির্ধারণের জন্য। একটি রৈখিক রিগ্রেশন মডেল ব্যবহার করে গ্লুকোজের মাত্রা নির্ণয় করা হয়েছে, যা সেন্সরের প্রতিফলন সহগের মান এবং গ্লুকোজের মাত্রার মাঝে সম্পর্ক স্থাপন করে। আঙ্গুলের বিভিন্ন টিস্যুর পুরুত্ব পরবর্তনের প্রভাব নিয়ে বিশ্লেষণ সম্পাদিত হয়েছে। সেন্সরটি একটি উল্লেখযোগ্য সংবেদনশীলতা প্রদর্শন করে যার মান হলো ১.৭৯২ ডেসিবেল প্রতি মিলিগ্রাম প্রতি ডেসিলিটার এবং এটি উচ্চ নির্ভুলতার সাথে গ্লুকোজের মাত্রা পরিমাপ করতে সক্ষম যা গড় পরম আপেক্ষিক পার্থক্য (MARD) ও ক্লার্ক ত্রুটি গ্রিড বিশ্লেষণের দ্বারা নিশ্চিত হয়। সেন্সরটিতে সর্বোচ্চ ১-গ্রাম নির্দিষ্ট শোষণ হার (SAR) এর মান পাওয়া গিয়েছে ০.৫১৯ ওয়াট প্রতি কেজি যা ডিভাইসের রেডিও ফ্রিকোয়েন্সি নিরাপত্তা নিশ্চিত করে। এই সেন্সরটি অন্যান্য অত্যাধুনিক সেন্সরের তুলনায় উচ্চতর কর্মক্ষমতা প্রদর্শন করে।

ACKNOWLEDGEMENTS

In the name of Allah, the Most Gracious, the Most Merciful. All praise is due to Allah, the Lord of all worlds, and peace and blessings be upon His Messenger, Prophet Muhammad (peace be upon him), whose guidance and teachings have illuminated my path throughout this academic journey.

I extend my deepest gratitude to my supervisor Professor Dr. Md. Hossam-E-Haider, Department of Electrical, Electronic and Communication Engineering (EECE), Military Institute of Science and Technology (MIST) for his unwavering support, guidance and invaluable mentorship. His dedication, insightful feedback and encouragement have been instrumental in shaping the course of my research and academic pursuits. The author would also like to convey his sincere gratitude to esteemed faculty members of the Department of EECE for their invaluable suggestion and academic insights. Finally, the author extends his heartfelt thanks to his family and friends for their unyielding support throughout this academic endeavor.

TABLE OF CONTENTS

LIST OF FIGURES

LIST OF TABLES

LIST OF ABBREVIATIONS

3-D	Three-dimensional
AGC	Aqueous glucose concentrations
AI	Artificial intelligence
A/m	Ampere per meter
BGL	Blood glucose level
CSRR	Complementary split ring resonator
dBi	Decibels relative to isotropic
DNG	Double negative
DPS	Double positive
ELC	Electric LC
ENG	Epsilon negative
IDF	International Diabetes Federation
ISF	Interstitial fluid
LHM	Left Hand Materials
mg/dL	Milligrams per deciliter
mmol/L	Millimoles per liter
MIR	Mid infrared
MNG	Mu negative
MARD	Mean absolute relative difference
NIR	Near infrared
OCT	Optical coherence tomography
RF	Radio frequency
R^2	Correlation coefficient
SAR	Specific absorption rate
SIW	Substrate-integrated waveguide
SRR	Split ring resonator
SUT	Sample under test
UWB	Ultra-wideband
VNA	Vector network analyzer
WHO	World Health Organization
W/kg	Watt per kilogram

LIST OF SYMBOLS

α	Broadening parameter
ε_r	Complex relative permittivity
ω	Angular frequency
χ	Glucose concentration
ε_∞	High frequency permittivity
ε_{stat}	Static permittivity
ε_0	Free space permittivity
ε_{reff}	Effective dielectric constant
$\Delta\varepsilon$	Magnitude of dispersion
σ_s	Ionic conductivity
τ	Relaxation time
μ_0	Free space permeability
λ_0	Free space wavelength
D_p	Penetration depth
f_r	Resonant frequency
g	Split gap
h	Substrate thickness
k_0	Wave number
L_P	Length of the patch
L_c	Length of inset cut
ΔL	Normalized extension of length
R_O	Radius of outer ring

R_I	Radius of inner ring
S_{11}	Reflection coefficient
S_{21}	Transmission coefficient
$\tan(\delta)$	Loss tangent
W_P	Width of the patch
W_L	Width of the microstrip line
W_C	Width of inset cut

CHAPTER 1

INTRODUCTION

1.1 Overview

The growing rate and potential severity of diabetes, a metabolic condition, has emerged as a significant worldwide health issue. This physiological state occurs when the body's capacity to maintain equilibrium of blood glucose levels (BGL) is compromised, resulting in enhanced concentrations of glucose in the blood circulatory system. The severity of diabetes displays variations from case to case, whereby cases that are not properly treated present an elevated risk of consequences, including cardiovascular illnesses, kidney dysfunction, nerve damage, hypertension, slower healing process etc.

There exist two primary classifications of diabetes, namely type 1 and type 2. Type 1 diabetes is identified by a deficiency in the generation of insulin by individuals, whereas type 2 diabetes is mostly attributed to insulin resistance, wherein the body's cells exhibit reduced responsiveness to insulin. Diabetes is a chronic disease and there is currently no recognized treatment. However, the successful management and control of diabetes necessitate the implementation of many strategies. These include the maintenance of a well-balanced diet, regular engagement in physical exercise, diligent monitoring of blood sugar levels, adherence to prescribed medications, and in certain instances, the administration of insulin injections. These measures enable individuals to effectively manage their health and reduce the likelihood of experiencing adverse long-term problems related to diabetes.

1.2. Motivation of the Research

According to the 2021 report from the International Diabetes Federation (IDF), there were 536.6 million individuals affected by diabetes. It is estimated that this figure will increase to 642.7 million by 2030 and rise to 783.2 million by 2045. In 2021, the global death toll from diabetes reached 6.7 million people. A summary of Estimated total number of adults (20 ~ 79 years) with diabetes in different regions around the world is illustrated in Fig. 1.1 [1]. Another investigation conducted by the World Health Organization (WHO) reveals that diabetes has affected 8% of Bangladesh's entire population and it is responsible for 3% of deaths across all age groups [2].

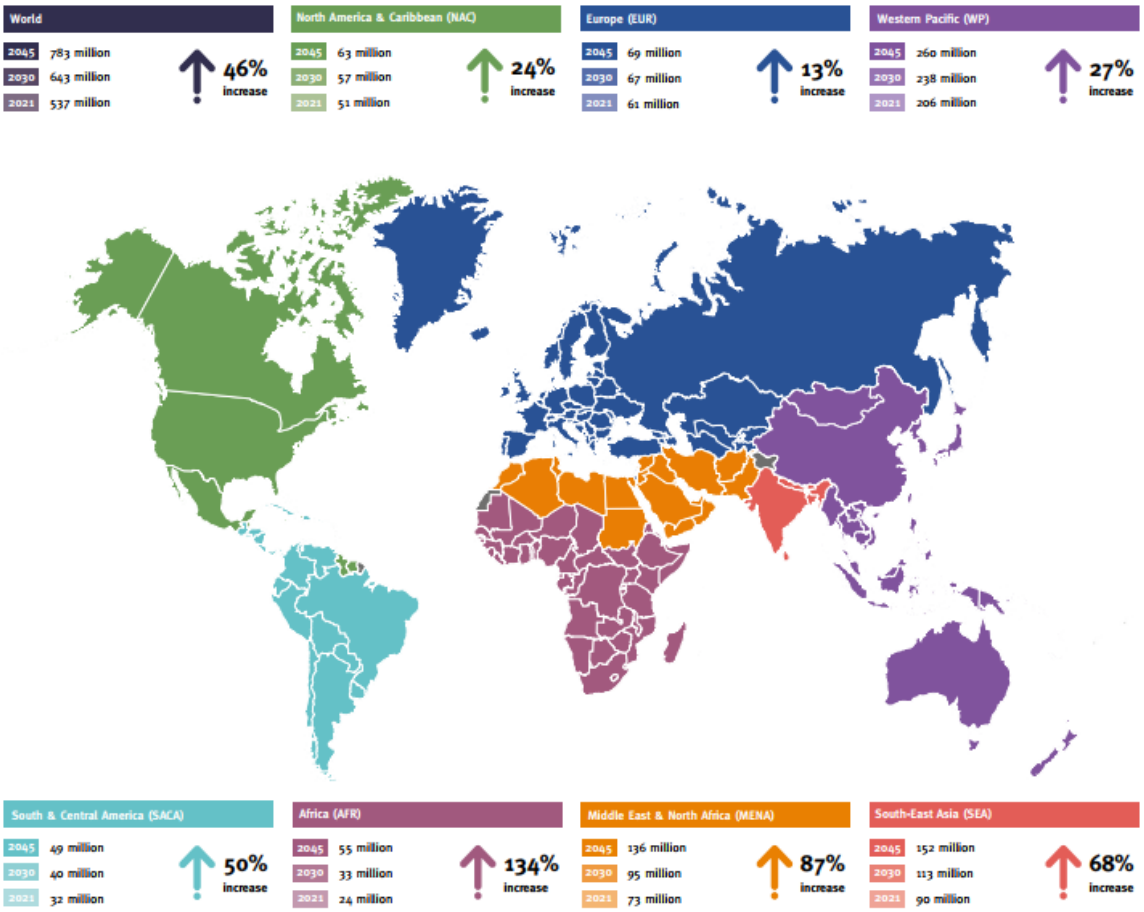

Fig. 1.1. Global diabetes prevalence in 2021 and estimation for 2030 and 2045 [1].

The most popular method to measure BGL is blood glucose meters (Glucometers) where a tiny drop of blood from fingertip is taken on a test strip as shown in Fig. 1.2. Although this procedure demonstrates an acceptable degree of precision, it is not without its drawbacks, particularly in relation to patient experience. Some patients may experience pain and discomfort, as well as an increased chance of infection. Additionally, these devices do not facilitate reusability, hence imposing financial burdens on consumers who require regular usage. Hence, there is a growing demand for non-invasive techniques to assess glucose levels.

(a) (b)

Fig. 1.2. (a) Glucometer with test strips. (b) Methodology for finger piercing: (1) Lancet needle, (2) Extracted blood is taken to the strip, (3) BGL reading display on the screen.

1.3. Objectives of the Research

This thesis aims to design and analyze a metamaterial based microwave sensor for non-invasive determination of glucose concentration, in response to the increasing demand in developing convenient blood glucose monitoring devices for the diabetic community. In the perspective of the aforementioned, the specific objectives of this research include:

(i) To design a biosensor based on metamaterial inspired microstrip patch antenna for determining blood glucose concentration.

(ii) To analyze the performance of the proposed biosensor by determining glucose concentration in an aqueous solution through simulation.

(iii) To verify the performance of the proposed biosensor by determining the blood glucose concentration in a designed human finger model.

1.4. Organization of the Research

The research presented throughout this thesis is structured into six chapters, organized as follows:

CHAPTER 1 - INTRODUCTION: An overview is presented regarding the fundamentals of diabetes, its severity and techniques of treatment. The present prevalence of diabetes globally

and in Bangladesh is examined. Subsequently, the need for the development of a non-invasive blood glucose monitoring system is explained. The specific objectives of the thesis are discussed. Finally, the arrangement of the research is presented.

CHAPTER 2 – LITERATURE REVIEW: The discussion focuses on various non-invasive techniques that utilize optical and bio fluid based approaches. Next, different methods of non-invasive glucose detection using RF/Microwave technology are discussed. The chapter also includes a summary of the mentioned microwave-based techniques.

CHAPTER 3 - DIELECTRIC PROPERTIES ESTIMATION: An analysis is conducted on the Debye and Cole-Cole relaxation models. Determination of the dielectric characteristics of aqueous glucose solutions employing Debye model is explained. An overview of the different tissues comprising the human finger model is presented. Lastly, the prediction of electromagnetic properties of the finger tissues is analyzed using Cole-Cole relaxation model.

CHAPTER 4 - SENSOR DESIGN AND ANALYSIS: The design of the microstrip patch antenna is explained. An analysis is presented to determine the dimensions of the CSRR unit cell by evaluating its impact on the sensor. The properties of the antenna are analyzed in order to define the sensing zone. A comprehensive investigation of the metamaterial properties was elaborated to demonstrate its significance in the glucose sensing operation.

CHAPTER 5 - RESULTS AND DISCUSSIONS: This chapter outlines the determination of glucose concentration from aqueous solution and blood glucose concentration from the finger model by analyzing the S_{11} parameter the microwave sensor. The impact of changing finger tissue thickness is also explained. The sensor's accuracy is assessed through the use of MARD and Clarke error grid analysis. The sensor's RF safety on the human body is also evaluated by computing the SAR of the sensor. Then comparison between the proposed sensor and other state-of-the-art sensors is provided.

CHAPTER 6 - CONCLUSION: Insightful conclusions are discussed. The limitations of the work are acknowledged and therefore, future recommendations are suggested.

CHAPTER 2

LITERATURE REVIEW

2.1 Non-Invasive Optical Methods

Several approaches have been implemented for non-invasive detection of glucose level. For instance, optical methods such as near infrared (NIR) and mid infrared (MIR) spectroscopy have been proposed where the NIR and MIR signals can effectively penetrate inside body tissues and quantify glucose concentration using the reflection or transmission method [3] [4]. However, there is a need for further enhancement of the sensor's sensitivity and accuracy. Optical polarimetry is another method that involves the rotation of a polarized beam of light due to the presence of a glucose solution. The deflection angle of polarized light is varied according to the variation in glucose level, indicating that changes in glucose level can be determined by analyzing the deflection angle [5]. Nevertheless, the presence of cloudy material causes scattering of polarized light, hence impacting the sensor's robustness and reproducibility.

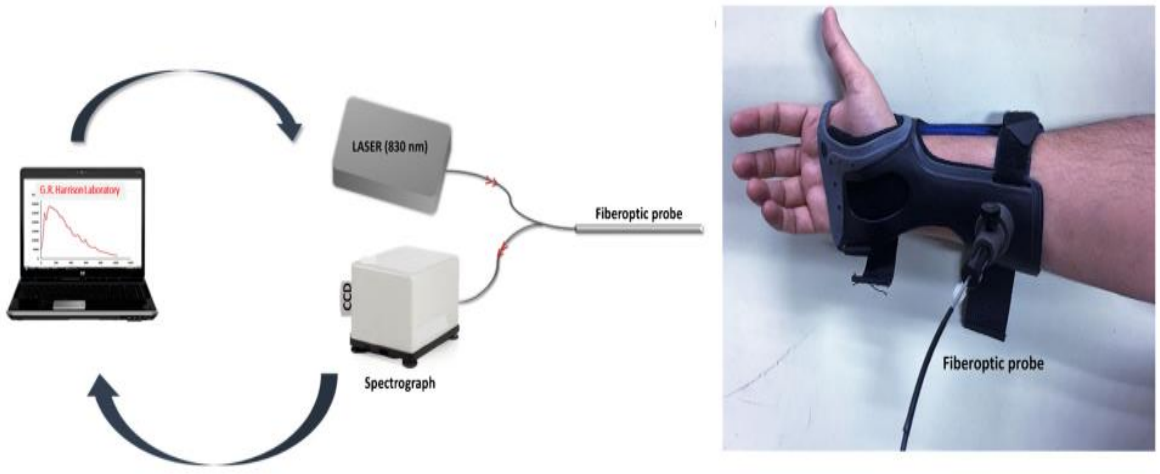

(a) (b)

Fig. 2.1 (a) Layout of Raman spectroscopy system. (b) A wrist support to hold the fiberoptic probe. [6].

Raman spectroscopy is capable of detecting the fundamental vibrations of particles and offers advantages such as decreased interference and measurement error compared to alternative optical techniques [6] [7]. Schematic of a Raman spectroscopy system is illustrated in Fig. 2.1 (a). An experimental setup where a wrist support equipped with a small opening designed

for mounting the probe is depicted in Fig. 2.1 (b). But the Raman spectrum is significantly influenced by the presence of background noise in the surrounding environment which is a limitation of such system. Optical coherence tomography (OCT) is an imaging technology where OCT signal experiences alterations in optical reflection inside biological tissues [8] [9]. This method has several advantages like enhanced resolution, elevated signal to noise ratio and increased depth of penetration. However, this method is significantly influenced by fluctuations in skin temperature, obtains reduced precision in measurements and has limited potential for reuse.

2.2 Non-Invasive Bio Fluid Based Methods

Several bio fluid based electrochemical techniques have been suggested to facilitate the non-invasive detection of glucose levels in bio fluids such as saliva, tears, sweat, and interstitial fluid (ISF). Saliva possesses the benefit of being more easily extracted and collected compared to other bio fluids, making it suitable for use in non-invasive glucose sensors [10]. However, the drawbacks of these biosensors encompass the existence of obstructive pollutants, as well as issues with low sensitivity and accuracy. The primary benefit of the tear-based non-invasive glucose sensor lies in the reduced presence of interfering contaminants in tears, as well as the positive correlation between glucose levels in tears and blood glucose levels [11]. Nevertheless, this type of sensor typically produces heat leading to eye irritation and discomfort. Furthermore, the measurement precision failed to reach the clinical standards. Sweat can be readily gathered, and sweat-based sensors provide wearable devices for uninterrupted monitoring of glucose levels [12]. But prolonged exercise or intense heat is necessary to cause sweat to appear on the skin, neither of which is good for diabetic patients. Additionally, sweat sensors exhibit reduced sensitivity as a result of the lower glucose levels present in sweat. The ISF glucose sensor utilizes transdermal Reverse Iontophoresis (RI) technology to extract glucose. Fig. 2.2 (a) shows the paper battery attached to skin to generate electrochemical twin channels. The biosensor fully conforms to the skin to measure glucose level from ISF as depicted in Fig. 2.2 (b). The advantages of this method include a high concentration of glucose in the ISF and a strong correlation coefficient with blood glucose. As a result, its accuracy surpasses that of the other three methods. Nevertheless, the issue at hand is that while a greater current enhances the sensor's detection limit and sensitivity, the higher current also leads to increased skin irritation [13].

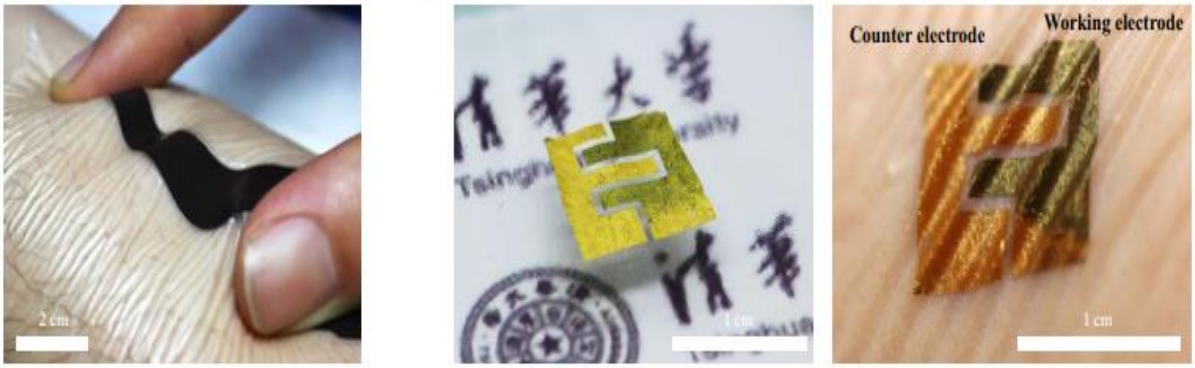

(a) (b)

Fig. 2.2. (a) The paper battery attached to the skin. (b) The ISF glucose sensor completely conforming the skin surface [13].

2.3 Non-Invasive Microwave Based Methods

Radio Frequency (RF)/Microwave based glucose biosensors have been extensively integrated due to their numerous advantages. RF/Microwave technology possesses the capability to penetrate human tissue to significant depths without inducing any adverse effects. Numerous microwave cavity-based sensors have been employed for the purpose of glucose detection. A proposed method for measuring blood glucose concentration involves the use of a sensor that features a cylindrical cylinder with a centrally positioned capillary tube [14]. Another research introduces an epsilon negative (ENG) unit-cell resonator consisting to two ring and horn shaped complementary geometries as represented in Fig. 2.3. A PDMS cavity is positioned in the sensing region to contain 2 μL sample with glucose concentration ranging from 20 mg/dL - 100 mg/dL [15].

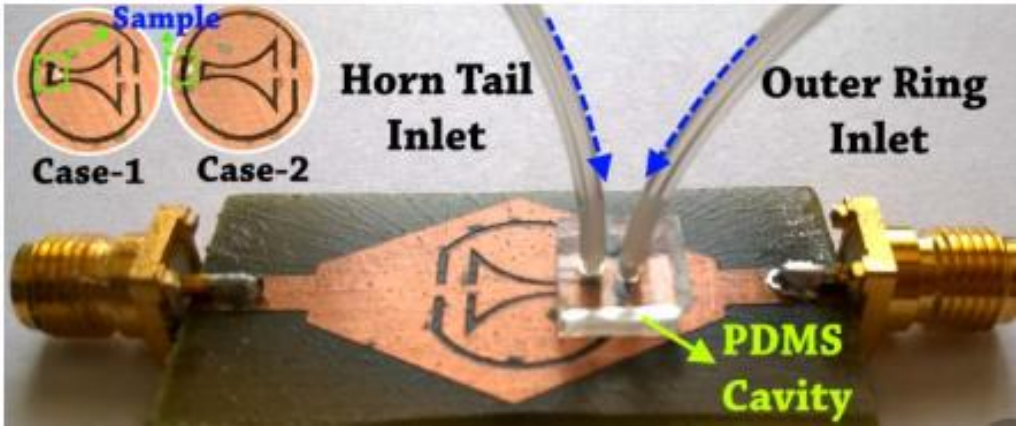

Fig 2.3. Configuration of an ENG unit-cell resonator with PDMS cavity to contain water and glucose concentrations [15].

Several biosensors that use microwave microprobes have been implemented for the measurement of glucose levels. A microwave dielectric resonator with a waveguide probe has been designed with the purpose of detecting fluctuations in glucose concentration within the range of 0 mg/dL to 300 mg/dL as illustrated in Fig. 2.4 [16]. The utilization of a dielectric resonator in conjunction with a near-field microwave microprobe is used for the purpose of quantifying the concentration of glucose in a solution containing glucose and NaCl [17].

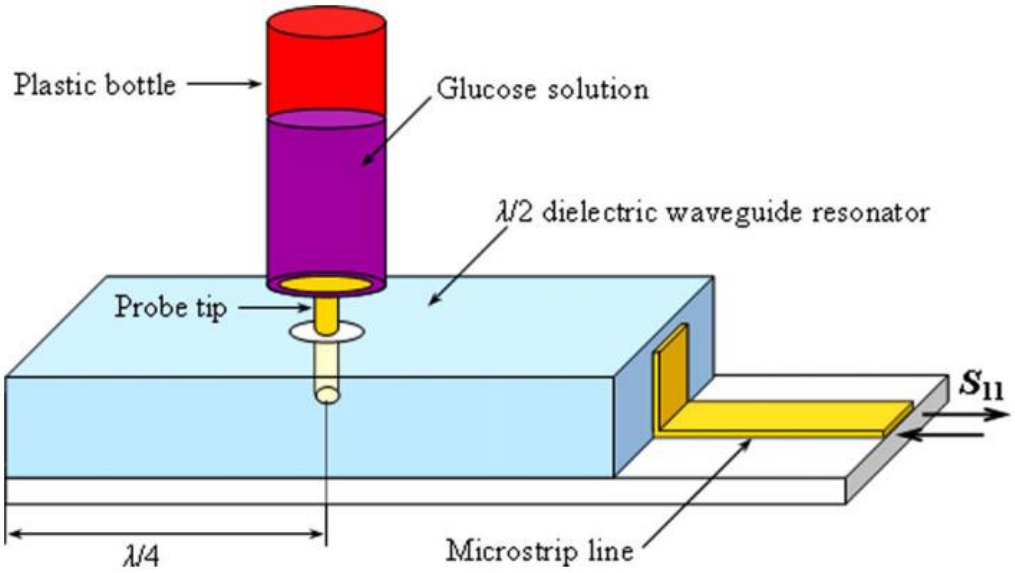

Fig. 2.4. Schematic diagram of $\lambda/_2$ dielectric resonator with metal probe tip to hold a plastic bottle containing glucose solution [16].

Substrate-integrated waveguide (SIW) based sensors have become prevalent in the context of liquid characterization. The SIW technology is used to develop a sensor capable of measuring BGL from the fingertip [18]. A recent study introduces a circular SIW sensor that incorporates a glass capillary for the purpose of analyzing the dielectric characteristics of aqueous solutions as shown in Fig. 2.5 [19].

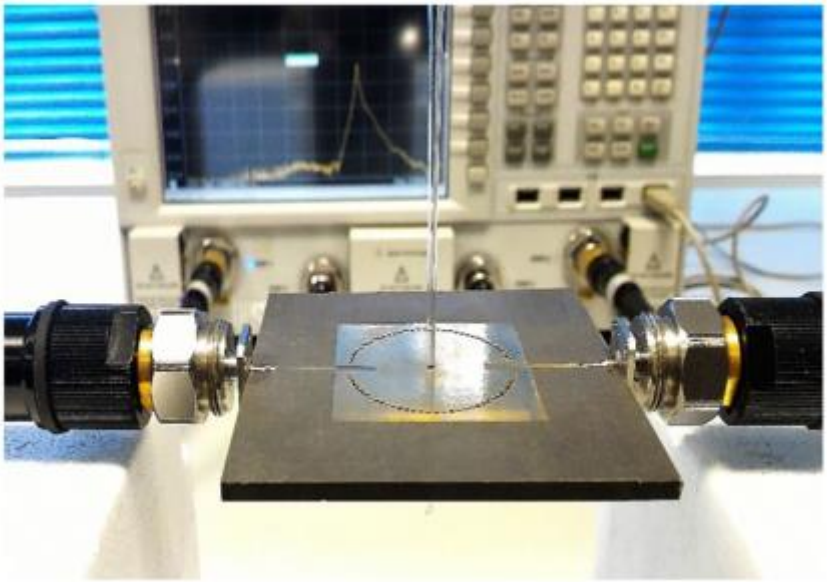

Fig. 2.5. The configuration of the sensor consisting of circular SIW with microcapillary channel [19].

Antennas, mainly microstrip patch antennas are utilized not only to transmit and receive signals, but also find application in glucose detection. A sensor utilizing an antenna is constructed to emit an endfire beam to conduct in-vitro and in-vivo glucose level measurement [20]. In another study various microstrip antenna sensors were used to assess BGL based on the return loss of the sensors. The front and back view of a fabricated ultra-wideband (UWB) antenna and front view of a spiral shaped antenna is illustrated in Fig. 2.6 (a) and Fig. 2.6 (b) respectively. The researchers subsequently conducted a comparative analysis of different sensors [21].

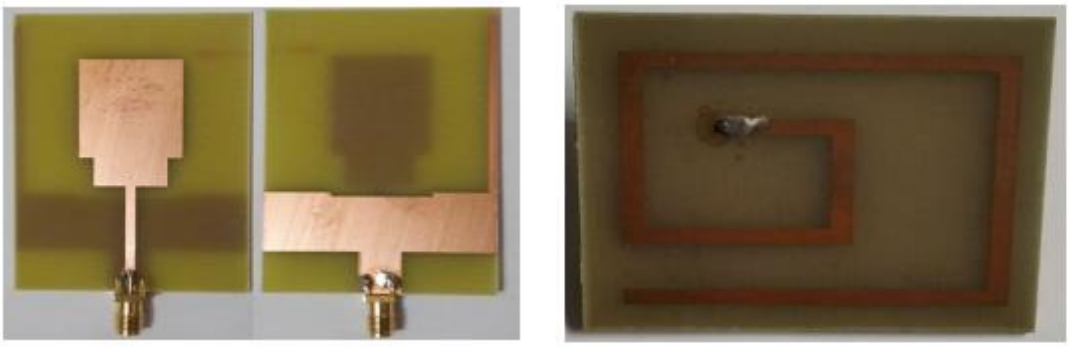

(a) (b)

Fig 2.6. Structure of (a) UWB, (b) spiral shaped antennas for glucose detection [21].

Microwave planar resonant sensors are well recognized as highly efficient sensors within the realm of RF/Microwave based approaches. Certain planar sensors rely on resonance frequency as the primary sensing parameter. A novel electric LC (ELC) resonator is introduced, which consists of a glass capillary filled with a solution containing both aqueous and blood glucose components. Fig. 2.7 (a) depicts the ELC resonator connected with the vector network analyzer (VNA). Collected goat blood samples of different concentrations from 100 mg/dL to 500 mg/dL are taken in the EDTA tubes as shown in Fig. 2.7 (b). The empty and blood-filled glass capillaries are illustrated in an enlarged view in Fig. 2.7 (c) [22]. Another study involved an examination of an interdigital structure that was integrated onto a coplanar waveguide transmission line. This analysis focused on various parameters of the sensor, including resonant frequency, peak frequency, impedance, resistance, and reactance [23].

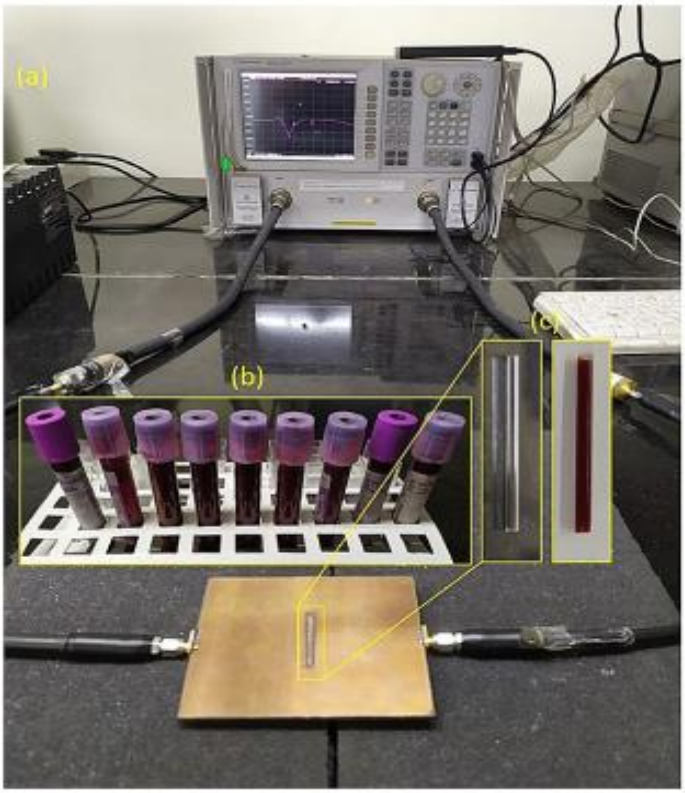

Fig. 2.7. (a) ELC resonator based sensor connected with the VNA. (b) Goat blood samples of different concentrations. (c) Empty and blood-filled glass capillary [22].

.

Different resonant sensors have been deployed for glucose sensing by measuring the amplitude of the S parameter. For instance, a microwave sensor has been proposed for the continuous monitoring of glucose levels, incorporating a metamaterial structure known as

CSRR. The microstrip feed-line and CSRR structure is depicted in Fig. 2.8 (a) and Fig. 2.8 (b) respectively. The sensor performs temperature correction by analyzing the experiment in stable and varying temperatures [24]. A microwave sensor comprised of two cells of circular Split ring resonator (SRR) with a liquid holder is introduced. Those resonators are coupled to a coplanar line creating a two-port network to measure aqueous glucose concentrations. Furthermore, an electrical prototype has been utilized to enhance the functionality of the sensing operation [25].

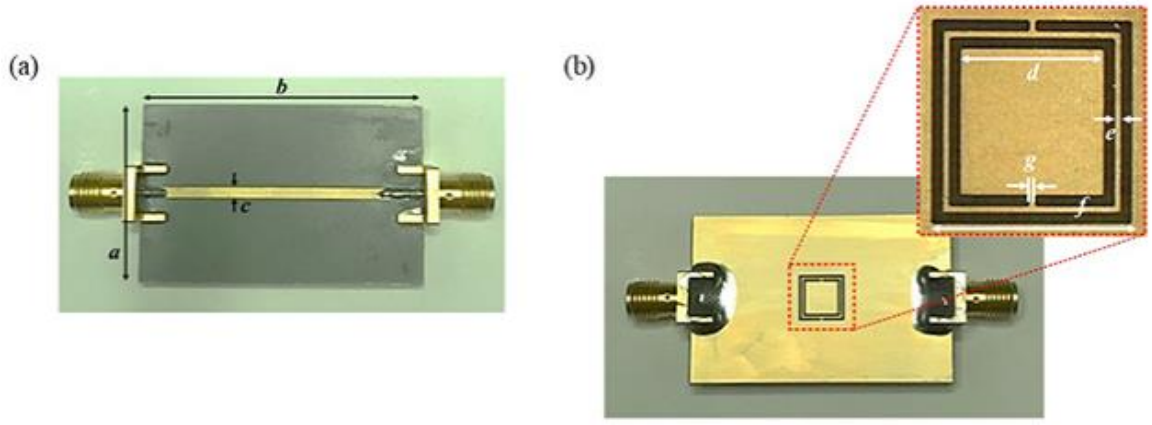

Fig. 2.8. (a) Microstrip Feed-line of the sensor. (b) Ground plane of the sensor and enlarged view of the CSRR region [24].

Several studies have been undertaken to investigate the quality factor of planar sensors. The Q factor was chosen as the sensing parameter for an open loop resonator, which is determined by the presence of a dielectric liquid container containing a microliter aqueous glucose solution which is shown in Fig. 2.9 [26]. The sensor of the paper [27] incorporates a transducer assisted by a metamaterial element called as SRR, which exhibits a robust field within the sensing zone to quantify glucose at various concentrations. Phase shift based planar sensors are also applied in glucose sensing. For example, a sensitivity of 2° phase shift per 0.1 mg/mL glucose concentration was achieved by a sensor consists of two-port microstrip line [28]. An overview of above mentioned microwave based glucose sensors are described in Table 2.1.

Fig. 2.9. (a) The microwave resonator with PTFE sample holder. (b) The sensor connected with VNA [26].

Table 2.1. An overview of different microwave glucose sensors

Ref.	**Sensor Structure**	**Operating Frequency (GHz)**	**Sensitivity**	**Remarks**
[14]	Cylindrical cavity	7.63	-	Detecting, tracking and measuring module
[15]	ENG unit-cell resonator	1.17	0.014 MHz/mgmL^{-1}	PDMS cavity
[16]	Dielectric resonator	2.15	-	Microwave waveguide probe
[17]	Near-field Microwave microprobe	4.5	0.005 dB/(mg/mL)	High Q dielectric resonator
[18]	Band-stop filter	5.46	0.02 MHz/mgdL^{-1}	SIW cavity, Fingerprint effect, modified SRR
[19]	Circular SIW	4.4	-	Resonant perturbation method, Any material charaterization
[20]	Spoof surface plasmon polarization sensor	8.9	150 MHz/mgmL^{-1}	Coplanar Waveguide
[21]	Microstrip antenna	4.7, 3.4, 1	-	Spiral, Ultra-wideband, Narrowband antenna

[22]	Complementary electric LC resonator	1.64	18.5 KHz/mgdL^{-1}	Glass capillary, Reusable
[23]	Coplanar interdigital structure	3.90	S_{11} – 0.0153 dB/(mg/mL) S_{21} – 0.005 dB/(mg/mL)	PDMS cavity, Non-reciprocal
[24]	Single CSRR	2.42	0.0153 dB/(mg/mL)	Microfluidic channel, Temperature corrected
[25]	Two cells of circular SRR	1.80	0.042 dB/(mg/mL)	In vitro test, Clarke error grid
[26]	Single SRR	5.16	-	Q factor, PTFE sample holder
[27]	Asymmetric single SRR	4.50	-	Q factor, High electric field confinement
[28]	Two port microstripline resonator	4.88	2° phase change per 10 mg/dl	Taper ground plane

Nevertheless, a significant drawback of the preceding sensors is their limited sensitivity, resulting in low accuracy when detecting glucose levels. One further obstacle faced by microwave sensors is the issue of inadequate selectivity, which refers to their limited capacity to measure the concentration of glucose in a solution amongst the presence of other elements.

This study presents a sensor adopting a microstrip patch antenna that incorporates a metamaterial element which is CSRR. The objective of this sensor is to measure the concentration of glucose in aqueous solutions and blood within the range of 50mg/dL to 300 mg/dL. The determination of the sensing zone is based on the area surrounding the CSRR, which possesses the capability to accumulate a significant concentration of high electric field. The sensitivity of this sensor is remarkable, determining at 1.792 dB/(mg/mL). The sensor under consideration also demonstrates a significant correlation between the computed glucose concentrations and the corresponding actual values.

CHAPTER 3

DIELECTRIC PROPERTIES ESTIMATION

3.1 The Theory of Dielectric Relaxation

A dielectric substance refers to an electrical insulator that does not allow for the free movement of internal electrical charges and can become polarized when an electric field is exerted. The word "absolute permittivity," also known as "permittivity," quantifies the extent to which a dielectric medium is influenced by an applied electric field. Dielectric polarization occurs when an electric field is applied to a dielectric, causing the displacement of electric charges from their usual stationary location in the material. Positive charges will shift towards the field, whereas negative charges will move in the opposite direction. The displacement of the charged particles will also generate an intrinsic electric field that opposes the applied electric field. Fig. 3.1. illustrates the impact of polarization on a dielectric material under the influence of an electric field.

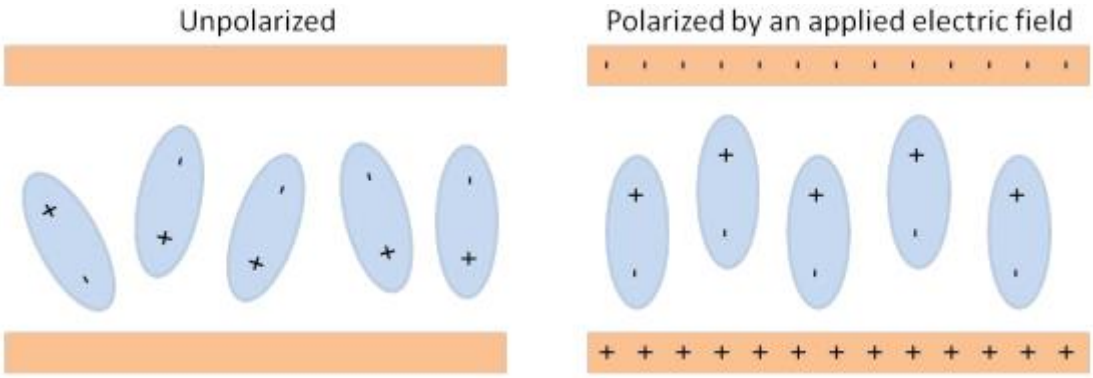

Fig. 3.1. The polarization phenomenon in the presence of an electric field on a dielectric material.

The electric displacement field, D, characterizes the influence of an electric field, E, on the alignment of electric charges and is described as:

$$D = \varepsilon_0 E + P_d \tag{3.1}$$

Here, P_d is the polarization density which represents the induced dipole moment in the material. The constant ε_0 denotes the permittivity in free space.

When a dielectric material displays an immediate response to variations in the electric field, it implies that the polarization density will exhibit a linear dependence on the electric field. The

relationship between polarization density and electric field can be expressed as:

$$P_d = \varepsilon_0 \chi_e E \tag{3.2}$$

Here, χ_e is known as electric susceptibility, which quantifies the level of polarization exhibited by dielectrics when subjected to an external electric field. The electric susceptibility can be expressed in terms of relative permittivity as:

$$\chi_e = \varepsilon_r - 1 = \frac{\varepsilon}{\varepsilon_0} - 1 \tag{3.3}$$

The polarization of a material does not exhibit an immediate reaction to the applied electric field and is dependent upon the frequency. Therefore, the polarization density is a function on angular frequency, ω and can be expressed as:

$$P_d(\omega) = \varepsilon_0 \chi_e(\omega) E(\omega) \tag{3.4}$$

Due to the frequency dependence of susceptibility, χ_e, the permittivity will similarly exhibit frequency dependence. The complex relative permittivity can be mathematically described as a function of the angular frequency $\omega = 2\pi f$ and the concentration of the material χ.

$$\varepsilon_r(\omega, \chi) = \varepsilon_r'(\omega, \chi) - j\varepsilon_r''(\omega, \chi) \tag{3.5}$$

Here, The real part, denoted as ε_r', represents the energy stored within the medium, while the imaginary part, denoted as ε_r'', represents the loss of energy in the medium. At lower frequencies, the permittivity exhibits minimal variation and remains in proximity to its static or low-frequency value. Nevertheless, at higher frequencies, the permittivity can undergo significant changes as a result of the reaction of the material's dipoles to the rapidly varying electric field.

The loss tangent is a frequency dependent measure of the energy dissipation in a dielectric substance when it is exposed to an electric field. It is represented as:

$$\tan(\delta) = \frac{\varepsilon_r''(\omega, \chi)}{\varepsilon_r'(\omega, \chi)} \tag{3.6}$$

Dielectric relaxation is the delay in molecular polarization with respect to an alternating electric field in a dielectric medium. The Debye equation is used to describe the relaxation response from the alignment of electric dipoles in reaction to an externally applied electric field. The Debye model introduces a relaxation time, denoted as τ, which serves as a measure of the time required for the dipoles to arrange themselves with the external electric field. The mathematical expression representing the Debye relaxation model is defined as follows [29]:

$$\varepsilon_r(\omega,\chi) = \varepsilon_\infty(\chi) + \frac{\varepsilon_{stat}(\chi) - \varepsilon_\infty(\chi)}{1 + j\omega\tau(\chi)} + \frac{\sigma_s}{j\omega\varepsilon_0} \tag{3.7}$$

$$\tan(\delta) = \frac{\{\varepsilon_{stat}(\chi) - \varepsilon_\infty(\chi)\}\omega\tau(\chi)}{\varepsilon_{stat}(\chi) + j\varepsilon_\infty(\chi)\omega\tau(\chi)} \tag{3.8}$$

These equations include the variables ε_{stat}, ε_∞ and σ_s, which represent the static permittivity, infinite permittivity and ionic conductivity respectively. For low-conductive materials such as glucose, the term $\frac{\sigma_s}{j\omega\varepsilon_0}$ can be disregarded.

The Cole-Cole model is characterized as an enhanced version of the Debye model. The Cole-Cole model incorporates a parameter, α which measures the extent of non-exponential behavior in the relaxation phenomenon. The parameter α can take value between 0 and 1. When the value of α is set to 0, the model simplifies to the Debye model. The first order Cole-Cole relaxation model is mathematically described by the following equations [30]:

$$\varepsilon_r(\omega) = \varepsilon_\infty + \frac{\Delta\varepsilon}{1 + (j\omega\tau)^{(1-\alpha)}} + \frac{\sigma_s}{j\omega\varepsilon_0} \tag{3.9}$$

$$\varepsilon_r'(\omega) = \varepsilon_\infty + \Delta\varepsilon \frac{1 + (\omega\tau)^{(1-\alpha)}\sin(\alpha\pi/2)}{1 + 2(\omega\tau)^{(1-\alpha)}\sin(\alpha\pi/2) + \omega\tau^{2(1-\alpha)}} \tag{3.10}$$

$$\varepsilon_r''(\omega) = \frac{\Delta\varepsilon(\omega\tau)^{(1-\alpha)}\cos(\alpha\pi/2)}{1 + 2(\omega\tau)^{(1-\alpha)}\sin(\alpha\pi/2) + \omega\tau^{2(1-\alpha)}} \tag{3.11}$$

3.2 Dielectric Properties of Aqueous Glucose Solution

The dielectric properties of a substance determine the manner in which waves propagate within that medium. Hence the dielectric properties of a given material serve as fundamental design parameters for the RF/microwave sensors. When a sensor comes in proximity to a tissue, the electromagnetic wave emitted by the sensor interacts with the tissue, thereby altering the frequency response of the sensor. If blood glucose concentration is changed, the dielectric properties of blood will also vary which can be determined using a microwave sensor. Approximately 50 percent of the total volume of human blood consists of water, along with components like glucose, sodium, calcium, potassium, chloride and others. Therefore, aqueous glucose solution can be considered as an approximation for blood in the initial phase of designing a microwave sensor, as it exhibits similar characteristics to blood. The first order Debye relaxation model is utilized in the literature to approximate the

dielectric properties of the aqueous glucose solution. The potential relationship between Debye parameters and glucose level may be derived from the following formulas [31]:

$$\varepsilon_{\infty}(\chi) \approx 5.38 + 30 \times 10^{-3} \chi \tag{3.12}$$

$$\varepsilon_{stat}(\chi) \approx 80.68 - 0.207 \times 10^{-3} \chi \tag{3.13}$$

$$\tau(\chi) \approx 9.68 + 0.23 \times 10^{-3} \chi \tag{3.14}$$

Table 3.1: Dielectric properties of aqueous glucose solution

Glucose concentration (mg/dL)	**Relative Permittivity**	**Loss tangent**
50	59.14	0.5672
100	59.54	0.5521
150	59.93	0.5373
200	60.33	0.5226
250	60.73	0.5081
300	61.13	0.4938

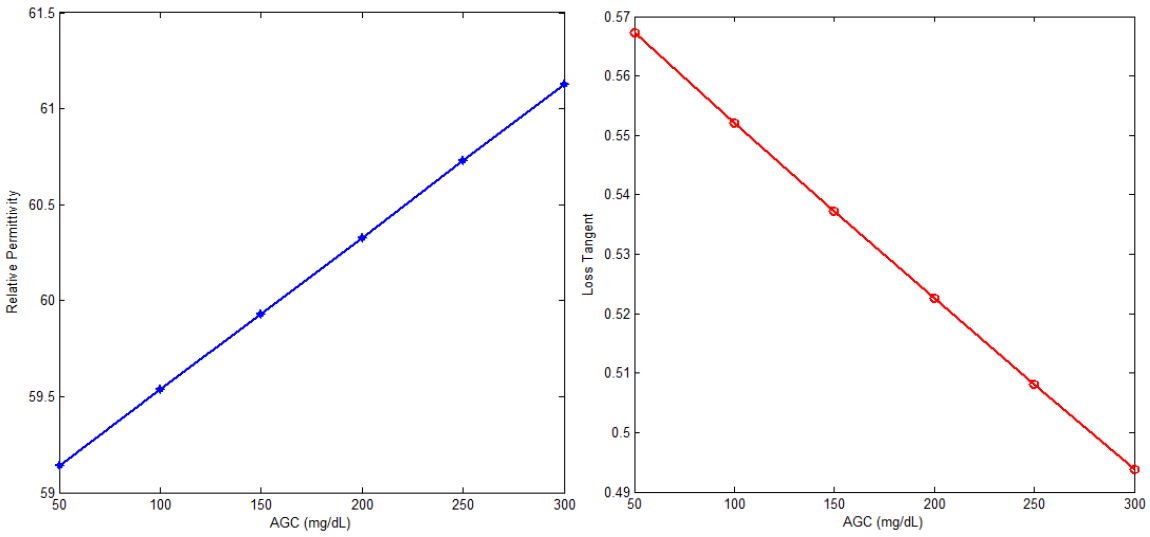

(a) (b)

Fig. 3.2. Estimated values of (a) relative permittivity and (b) loss tangent with fitted curve for different AGC using Debye relaxation model.

Table 3.1 presents the data corresponding to the relative permittivity and loss tangent of aqueous glucose solution with different concentrations. These values have been estimated

using the Debye relaxation model, particularly at the resonant frequency of the proposed sensor, which is 10.54 GHz. The predicted values of relative permittivity and loss tangent along with the fitted curve are depicted in Fig. 3.2.

The glucose concentration range examined in this study is from 50 mg/dL to 300 mg/dL. The rationale for selecting this range pertains to the possible diabetes level of individuals. The normal blood glucose level of an individual is less than 100 mg/dL (5.6 mmol/L) while fasting and less than 140 mg/dL (7.8 mmol/L) after meal. An extreme lower glucose level is known as hypoglycemia. Blood glucose level indicating hypoglycemia is typically less than 70 mg/dL (3.9 mmol/L) for fasting and less than 70-80 mg/dL (3.9-4.4 mmol/L) after meal. An extreme higher glucose level is termed as hyperglycemia. Blood glucose level indicating fasting hyperglycemia is greater than 100 mg/dL (5.6 mmol/L) and greater than 180 mg/dL (10.0 mmol/L) after meal. [32]. Therefore, the selected range encompasses the entire spectrum of glucose levels that can be typically observed in humans, spanning from exceptionally low to exceptionally high values.

3.3 Dielectric Properties of Human Finger Model

In this investigation, a simulation is conducted using a multi-layer human finger model in order to ascertain the BGL. Several recent research have presented various models for the structure of the human finger, which consist of multiple tissues [33] [34]. However, these studies have not provided a clear explanation for the selection of specific thicknesses for each layer. The human finger model proposed by Cebedio et al. has been considered in this study [35]. They estimated the layer thickness using ultrasound technology on the small finger of an actual human volunteer. The model encompasses six distinct biological tissues, including dry and wet skin, blood, fat, muscle, bone. Additionally, a nail has been incorporated at the top of the skin layer. Each layer is in the square shape with a side length of 3.3 mm, except for the nail layer, which has a width that is half of the other layers.

The anatomy of a typical human finger is illustrated in Fig. 3.3. Initially we need to take into account the impact of skin layers. Skin is mainly composed of three distinct layers: epidermis, dermis and hypodermis. In this model skin is modeled as consisting of two layers: dry skin and wet skin. The relative permittivity value of skin is high, similar to that of blood. Consequently, the electromagnetic wave experiences more attenuation inside this layer compared to other tissues.

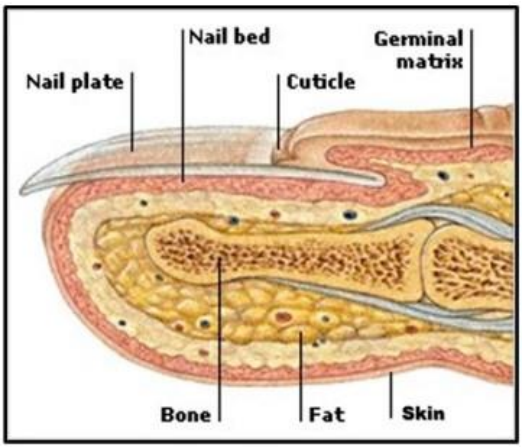

Fig. 3.3. Anatomy of a human finger.

The transportation of blood from the heart to the human finger occurs through the arteries, while the return of blood from the finger to the heart takes place via the veins. Capillaries are small blood channels which enable the connection between arteries and veins. Previous studies suggested the concept of blood as a single thick layer. Considering blood as a thick layer would simplify our task by allowing the sensor to effectively detect the dielectric characteristics of blood, resulting in enhanced sensitivity. However, the present model adopts a more realistic approach by defining blood as comprising three distinct and thin layers. The blood hematocrit is a crucial determinant of the dielectric characteristics of blood. Blood hematocrit is the proportion of red blood cells in the blood. At low frequencies, there is a significant variation in the dielectric constant due to changes in the hematocrit. The occurrence of this phenomenon diminishes at higher frequency as a result of the linear relationship between the real part of the dielectric constant [36].

The tissue of the muscle is accountable for both movement and keeping control of body position. Bone tissue fulfills a crucial role in the body by offering support and protection, ensuring the structural integrity of key organs, and serving as a storage site for minerals. The bone structure exhibits a number of holes, hence facilitating the elevated permeability of electromagnetic waves. Both muscle and bone tissues exhibit a high degree of transparency to microwaves. These waves can go through the tissues without much absorption. The layout of the human finger model used in the simulation is shown in Fig. 3.4.

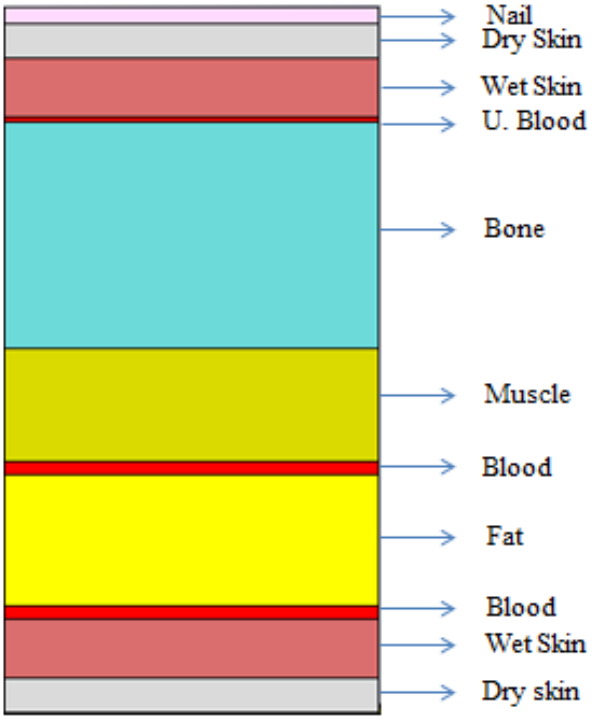

Fig. 3.4. Different layers of the human finger model.

The operating frequency of the sensor is a critical factor that significantly affects the penetration depth through the finger. The depth of penetration can be described by the following equation [37]:

$$D_p = \frac{\lambda_0}{2\pi\sqrt{2\varepsilon_r'}} \times \frac{1}{\sqrt{1+\left(\varepsilon_r''/\varepsilon_r'\right)^2}-1} \tag{3.15}$$

Here, λ_0 is denoted free space wavelength which decreases when the frequency increases ($\lambda = c/f$). To analyze the behavior of blood circulating in the finger, mainly penetration through skin and fat layer is required, while penetration via muscle and bone is of less importance. Moreover, research has demonstrated that the sensitivity of biosensors to changes in glucose concentrations is enhanced at higher frequencies. This makes it possible for blood and microwaves to interact more strongly [38]. Hence our choice of higher operating frequency (>10 GHz) is justified.

Biological tissues can be characterized as materials that exhibit frequency-dependent behavior and the dispersion relation is typically described by the Cole-Cole relaxation model. The Cole-Cole equations are utilized to estimate the dielectric characteristics of the layers present in the human finger model. The parameters included in the Cole-Cole model for the estimation of dielectric characteristics in different human tissue are presented in Table 3.2

[39]. An overview of the dielectric characteristics and thickness of different biological tissues is shown in Table 3.3.

Table 3.2: Parameters used in the Cole-Cole model

Tissue	ε_∞	**Δε**	**τ (PS)**	**α**	**σ**
Dry skin	4	32	7.23	0	0.0002
Wet skin	4	39	7.96	0.1	0.0004
Bone	2.5	10	13.26	0.2	0.0200
Muscle	4	50	7.23	0.1	0.2000
Fat	2.5	3	7.96	0.2	0.0100

Table 3.3: Overview of the finger tissues

Tissue	**Thickness**	**Relative Permittivity**	**Loss tangent**
Dry Skin	0.6	30.03	0.4150
Wet Skin	1.04	32.44	0.4473
Blood	0.25	Variable	Variable
Fat	2.3	4.56	0.2170
Muscle	2	41.87	0.4261
Bone	4	7.90	0.4582
Nail [40]	0.3	3	-
U. Blood	0.1	Variable	Variable

The parameters of Cole-Cole equation are a function of glucose concentration of blood, as shown by the following equations [41]:

$$\varepsilon_\infty(\chi) = 0.0099\chi^2 + 0.047\chi + 2.3 \tag{3.16}$$

$$\Delta\varepsilon(\chi) = -0.0093\chi^2 + 0.21\chi + 71 \tag{3.17}$$

$$\tau(\chi) = 0.0012\chi^2 + 0.23\chi + 8.7 \tag{3.18}$$

$$\sigma_s(\chi) = 0.0063\chi^2 - 0.14\chi + 2 \tag{3.19}$$

Here, χ represents blood glucose concentration, expressed in g/dL. The calculated dielectric properties of different concentrations of blood at 10.54 GHz, the resonant frequency of the sensor, are presented in Table 3.4. The estimated values of permittivity and loss tangent with the fitted curve are illustrated in Fig. 3.5.

Table 3.4: Dielectric properties of BGL

BGL (mg/dL)	**Relative Permittivity**	**Loss tangent**
50	52.08	0.5253
100	52.04	0.5259
150	52.01	0.5264
200	51.97	0.5269
250	51.94	0.5274
300	51.90	0.5280

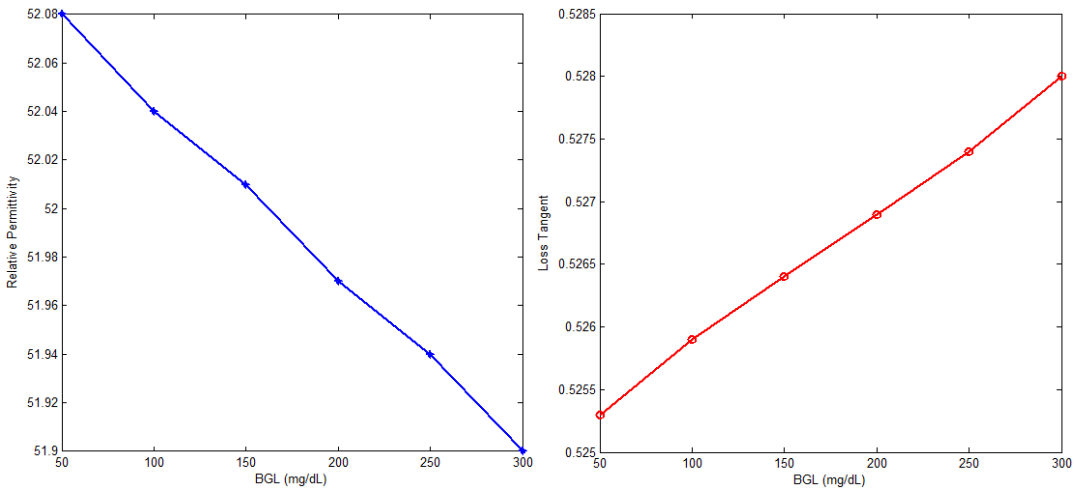

(a) (b)

Fig. 3.5. Predicted values of (a) relative permittivity and (b) loss tangent with fitted curve for different BGL using Cole-Cole relaxation model.

The investigation of dielectric characteristics as illustrated in Fig. 3.2 reveals that an increase in AGC results in an increase in relative permittivity and a decrease in loss tangent. However, a rise in BGL will result in a reduction in relative permittivity and an elevation in loss tangent which is depicted in Fig. 3.5. The heterogeneous nature of blood is responsible for the alteration in dielectric characteristics compared to that of a water solution. The complex relationship of different substances in blood creates a dynamic aspect, which affects dielectric characteristics in a way that is different from that of homogeneous water solutions. The aqueous and blood glucose solutions are the sample under test (SUT) in this analysis which will be created in CST Microwave studio as new materials. An in depth analysis will be performed to determine the correlation between the estimated dielectric properties of water and blood glucose concentrations and the resonance properties of the sensor which will be presented in the subsequent chapters.

CHAPTER 4

SENSOR DESIGN AND ANALYSIS

4.1 Principle of Metamaterial Based Antenna Sensor

An antenna has the capability to function as a sensing device while concurrently serving as a signal transmitter. This type of device is commonly known as an antenna sensor. Antenna sensors have been previously employed for various purposes including biomedical applications [20] [21]. In this study, a novel antenna sensor is designed utilizing a microstrip patch antenna for the purpose of non-invasive glucose level detection.

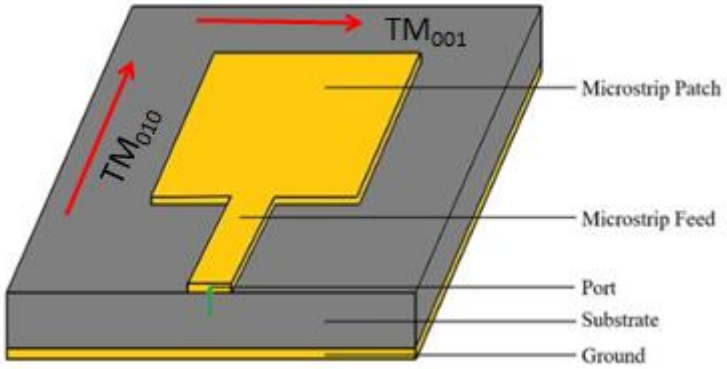

Fig. 4.1. The layout of microstrip patch antenna with fundamental resonant modes.

A microstrip patch antenna comprises four essential elements: a ground plane, a substrate, a radiation patch, and a transmission feed line. An electromagnetic resonator is formed by the conductive ground plane and the radiation patch, which are separated by a dielectric substrate. Consequently, a functional electromagnetic resonance cavity enables the emission of radiation at certain frequencies. The rectangular radiation patch antenna exhibits two fundamental resonant modes, namely the TM010 mode and the TM001 mode. The distinction between these two modes lies in the orientation of the electric current. In the TM010 mode, the current flows along the length of the radiating patch, whereas in the TM001 mode, it flows along the width of the patch as shown in Fig. 4.1. The radiating patch is powered by a microstrip feed line, where an input signal is given. The radiating patch either transmits or reflects this signal. The return loss of the microstrip patch antenna can be estimated by calculating the ratio of reflected power to incident power, which is sometimes referred to as the reflection coefficient or S_{11}. The working frequency of the antenna is determined by the

frequency at which the reflection coefficient is minimal. This means that very little energy is reflected by the antenna at this frequency and the majority of the incident power is radiated [42].

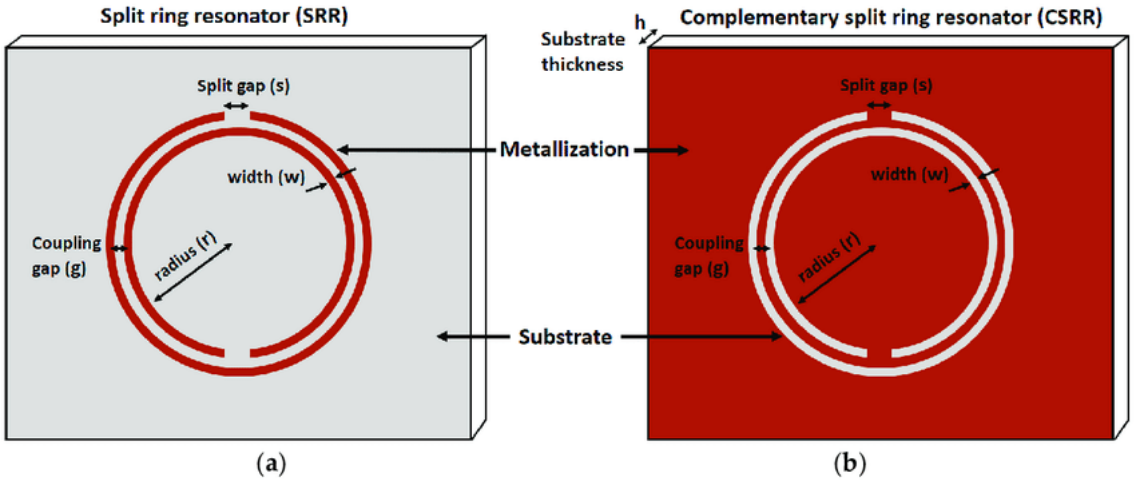

Fig. 4.2. Overview of SRR and CSRR structures [43].

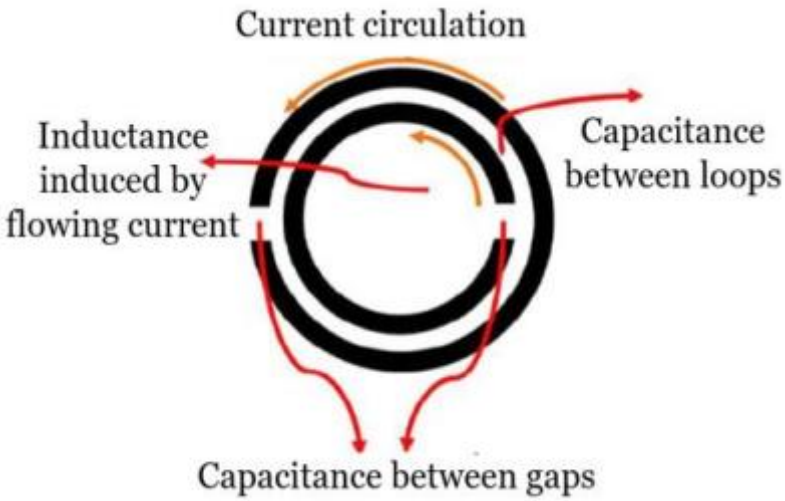

Fig 4.3. Electromagnetic characteristics of a CSRR cell [44].

The structure of typical SRR and CSRR are shown in Fig. 4.2. SRR and CSRR are frequently used as metamaterials in the context of material characterization operations. A SRR cell is composed of two metallic rings that have a split gap at opposite ends. There exists a space between both of the rings. Various shapes can be observed for SRR or CSRR, with circular and square forms being the most prevalent. The concept of CSRR can be understood as the inverse representation of SRR. In the case of SRR, rings are fabricated on the layer, whereas in the case of CSRR, rings are etched into the layer. The Electromagnetic behaviour of a

CSRR cell is depicted in Fig. 4.3. The electric field of SRR is localized within the narrow split gap. Conversely, in the context of CSRR, it is capable of confining highly intense electric fields inside a comparatively larger sensing area of the resonator, while simultaneously constraining the magnetic field between the slit traces. Consequently, this will result in improved sensitivity for the microwave-frequency analysis of lossy liquid samples [45]. For this reason, CSRR is selected as the metamaterial element for our proposed sensor.

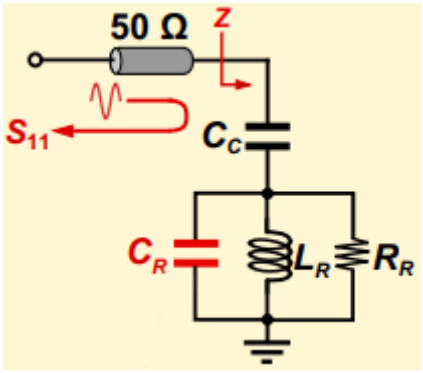

Fig. 4.4. Equivalent circuit of a CSRR based antenna sensor [46].

CSRR exhibits characteristics similar to those of a resonant electric dipole, and can therefore be represented as an RLC resonant circuit when an electric current flows through the loop which is presented in Fig. 4.4. The ring of the CSRR functions as an inductance L_R, while the split gap and separation between the outer and inner ring form a parallel capacitance C_R. The conductive and dielectric losses are represented by a resistance R_R. The effect of capacitive coupling that occurs between the 50 Ω microstrip transmission line and the CSRR can be express by a capacitance C_C. Thus, these structures resonate at a particular frequency when the oscillating electric and magnetic energy stored in the inductances and capacitances are in equilibrium. The resonant frequency of the structure can be expressed as [46]:

$$f_r = \frac{1}{2\pi\sqrt{L_R(C_R + C_C)}} \tag{4.1}$$

The aqueous and blood glucose solutions which have high permittivity and dielectric loss will interfere with the intensely distributed electric field surrounding the CSRR cell. The propagation of this intense electric field will interact with the glucose solution at the resonant frequency, resulting in a modification of the permittivity of glucose solution. The alteration in permittivity will result in a modification of the reflection coefficient of the sensor.

4.2 Antenna Design

The antenna based biosensor comprises a pair of circular CSRR rings which serves as the sensing region. The sensor design process involves utilizing a Rogers RT5880 substrate which possesses a relative permittivity (ε_r) value of 2.2 and a loss tangent (tan δ) value of 0.009. The thickness of the substrate is 1 mm. A rectangular patch of 17.3 mm in length and 21 mm in width is located at the center. The thickness of the metals used in the patch, microstrip line and ground of the antenna has been set at 0.05 mm. An inset-cut microstrip line feed technique is employed, whose width is calculated to be 3.1 mm in order to obtain an input impedance of 50 ohm. The length of the inset-cut is selected to be 5.8 mm which is about one third of the length of the patch. The antenna is designed to resonate at a frequency of 5.6 GHz. The simulation of the sensor is performed using CST Microwave Studio.

The outer ring of the CSRR has a radius of 3 mm, while the inner ring has a radius of 2.4 mm. The width of the rings, the spacing between them and split gaps, are all equal, measuring 0.3 mm. The schematic representation of the sensor is illustrated in Fig. 4.5. The key dimensions of the sensor are displayed in Table 4.1. The antenna dimensions were calculated using the following formulas [42]:

Width of the patch:

$$W = \frac{1}{2f_r\sqrt{\varepsilon_0\mu_0}}\sqrt{\frac{2}{\varepsilon_r+1}} \tag{4.2}$$

Effective dielectric constant:

$$\varepsilon_{reff} = \frac{\varepsilon_r+1}{2} + \frac{\varepsilon_r-1}{2}\left[1+\frac{12h}{W}\right]^{-\frac{1}{2}} \tag{4.3}$$

Normalized extension of length ΔL:

$$\frac{\Delta L}{h} = 0.412\frac{\left(\varepsilon_{reff}+0.3\right)\left(\frac{W}{h}+0.264\right)}{\left(\varepsilon_{reff}-0.258\right)\left(\frac{W}{h}+0.8\right)} \tag{4.4}$$

Length of the patch:

$$L = \frac{1}{2f_r\sqrt{\varepsilon_0\mu_0}\sqrt{\varepsilon_{reff}}} - 2\Delta L \tag{4.5}$$

Where, f_r = Resonance frequency

ε_r = Relative permittivity of the substrate

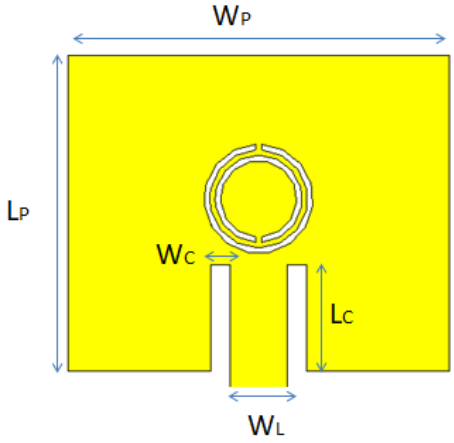

(a)

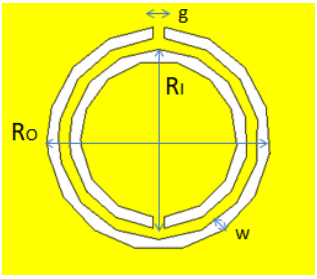

(b)

Fig. 4.5. (a) Simplified diagram of the sensor with CSRR. (b) Layout of the CSRR.

Table 4.1: Key parameters of the proposed sensor

Parameter	Description	Value (mm)
L_P	Length of the patch	17.3
W_P	Width of the patch	21
W_L	Width of the microstrip line	3.1
L_C	Length of the inset cut	5.8
W_C	Width of the inset cut	1.1
R_O	Radius of the outer ring	3
R_I	Radius of the inner ring	2.4
w	Width of both the rings	0.3
g	Split gap	0.3

4.3 CSRR Design

CSRR plays a crucial role in the attributes and functioning of the sensor. Fig. 4.6 presents a comparative analysis of the reflection coefficient (S_{11}) of the antenna, both with and without the inclusion of the CSRR. The antenna without CSRR exhibits three primary resonances, occurring approximately at frequencies of 5.6 GHz, 9.5 GHz, and 10.5 GHz. The application of the CSRR structure in antenna design leads to a notable alteration in the resonance characteristics. The resonant frequency of the sensor is determined by the dimensions of its length and width prior to loading of CSRR. But after the incorporation of CSRR, the parameters that govern the resonant frequency as well as amplitude of S parameters of our proposed sensor are the dimensions of the CSRR. Therefore an investigation about the design of CSRR is described in the subsequent section.

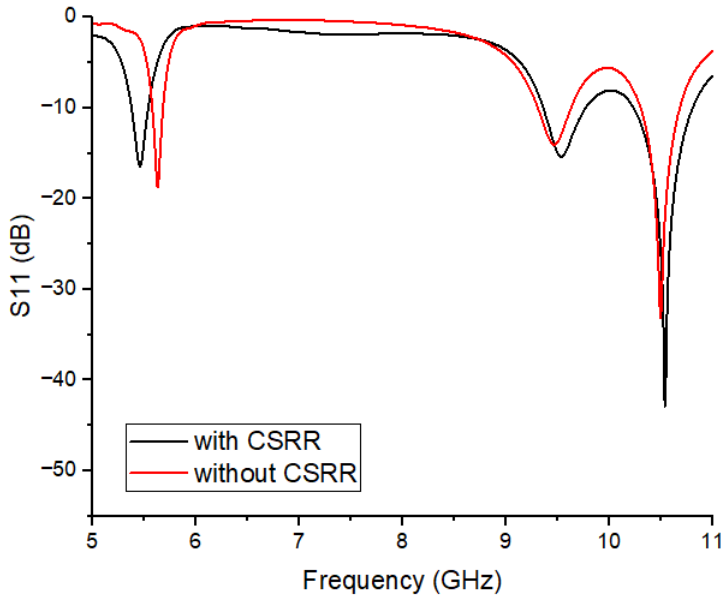

Fig. 4.6. Comparison of the reflection coefficient of the sensor with and without CSRR.

4.3.1 Determination of Number of CSRR Cells

Previous studies have used sensors featuring varying quantities of CSRR cells for the purpose of measuring glucose level [47] [45]. Various numbers of CSRR cells, specifically 1, 3, 4, 5, and 6, were employed in this research and thereafter an analysis of their respective S-parameters was conducted. Fig. 4.7 illustrates the configuration of CSRR cells within the sensor. The analysis of S-parameters of sensors equipped with different CSRR cells is shown in Fig. 4.8. The investigation reveals that the sensor equipped with a single cell configuration exhibits the lowest reflection coefficient (-42.9 dB) compared to sensors with multiple cells.

The sensor with triple cell yields a close approximation of the S_{11} value, determining at -41.4 dB. The results of the other three sensors are relatively modest compared to these two sensors. Therefore, the utilization of a higher number of cells does not effectively result in improved outcomes. Additionally, the selection of a single cell will contribute to a reduction in design complexity more effectively.

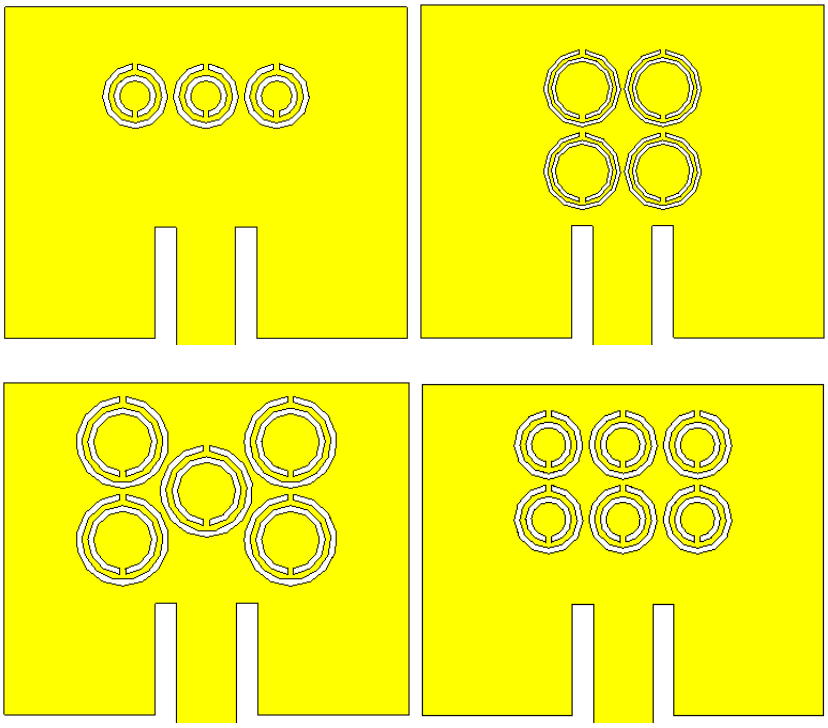

Fig. 4.7. The configuration of different numbers of CSRR cells in the glucose sensor.

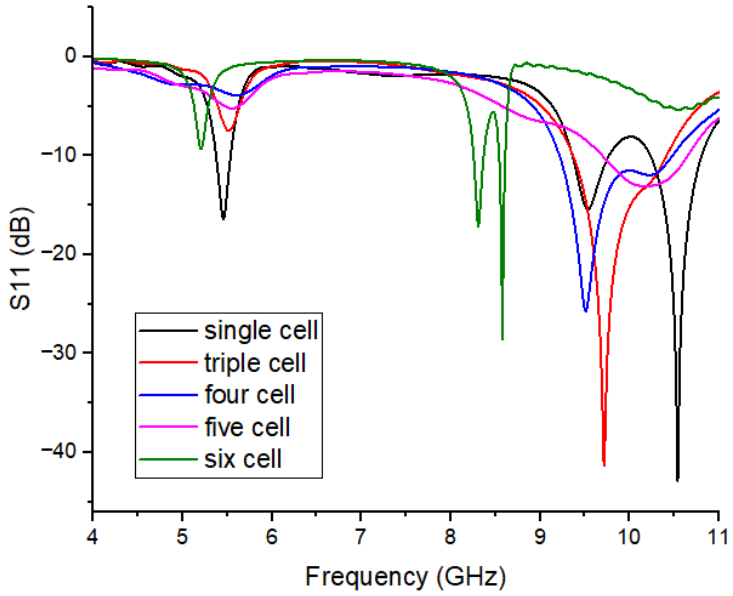

Fig. 4.8. Analysis of the S-parameters of sensors using various CSRR cells.

4.3.2 Determination of Radii of CSRR Rings

The radius of the CSRR rings is an important factor in the design aspect of the glucose sensor. The widths of both rings in a CSRR and the distance between them are equal. Consequently, when a particular radius for outer ring is selected, the radius of inner ring is adjusted accordingly. An investigation was conducted using different radii of rings of the CSRRs, as depicted in Fig. 4.9. The observation reveals that the CSRR, characterized by radius of 3 mm for outer ring and an radius of 2.4 mm for inner ring, has the most minimal reflection coefficient, -55.6 dB. Hence, the CSRR with this particular configuration has been chosen for the purpose of glucose detecting operation.

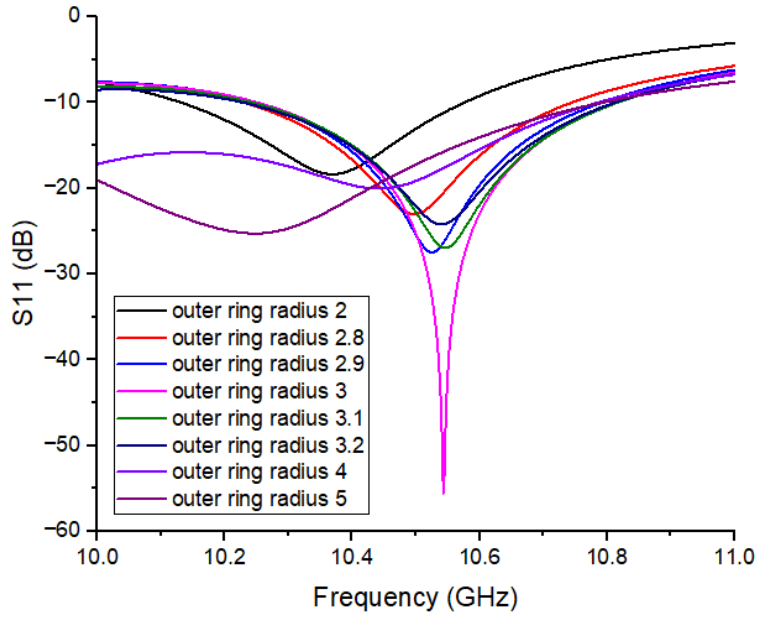

Fig. 4.9. Comparison of S_{11} (dB) at various CSRR ring radii.

4.3.3 Determination of the Location of CSRR Cell

The location of the CSRR cell is another significant design aspect. Various placements of the CSRR cell along the length of the patch have been taken into consideration. The performance study of the sensor, demonstrating the impact of different placements of the CSRR, can be observed in Fig. 4.10. The findings suggest that the sensor exhibits a minimal reflection coefficient of -53.4 dB when the distance from the center (DC) of the patch is 0.8 mm. Therefore, the optimal placement of the CSRR within the sensor is determined to be 0.8 mm above the centre of the patch.

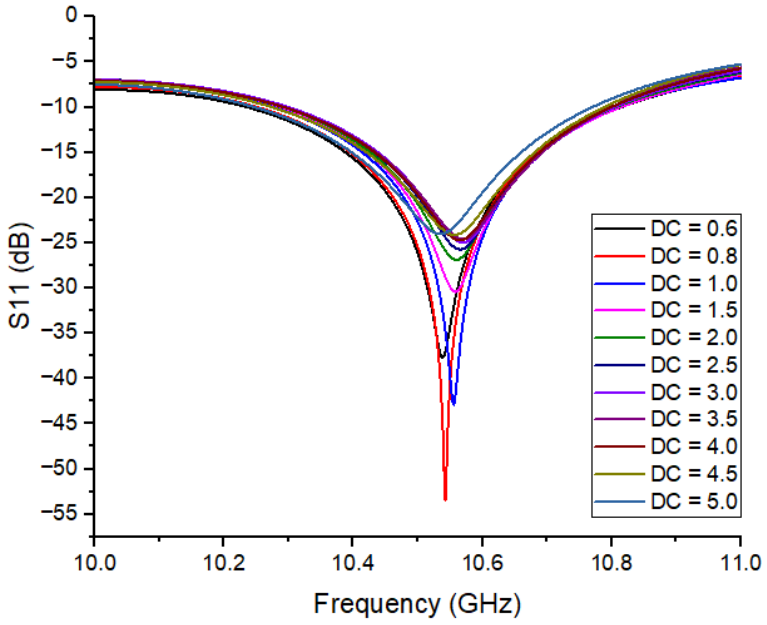

Fig. 4.10. Comparison of S_{11} (dB) at various CSRR location.

4.3.4 Determination of Optimum Shape of CSRR Cell

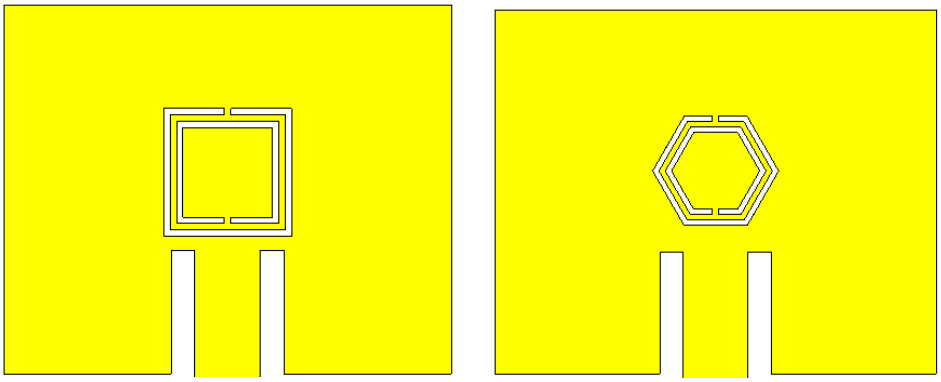

(a) (b)

Fig. 4.11. The schematic of the sensor with (a) square, (b) hexagonal CSRR.

In addition to the circular shape that is used for the CSRR cell, two other commonly used forms, namely the hexagonal and circular shapes, both having equal dimensions are evaluated and their characteristics are explored. Fig. 4.11 illustrates the layout of sensor with a square and a hexagonal shaped CSRR cell. The comparison of reflection coefficient of these sensors are shown in Fig. 4.12. It is the sensor with the circular CSRR has the lowest S_{11} value (-42.9 dB), whereas the square structure that demonstrates the closest proximity having the S_{11} value of -38.3 dB. The effect brought about by the hexagonal structure is unsatisfactory and

ignored. In consideration of this, we have completed the circular CSRR that was included in the sensor.

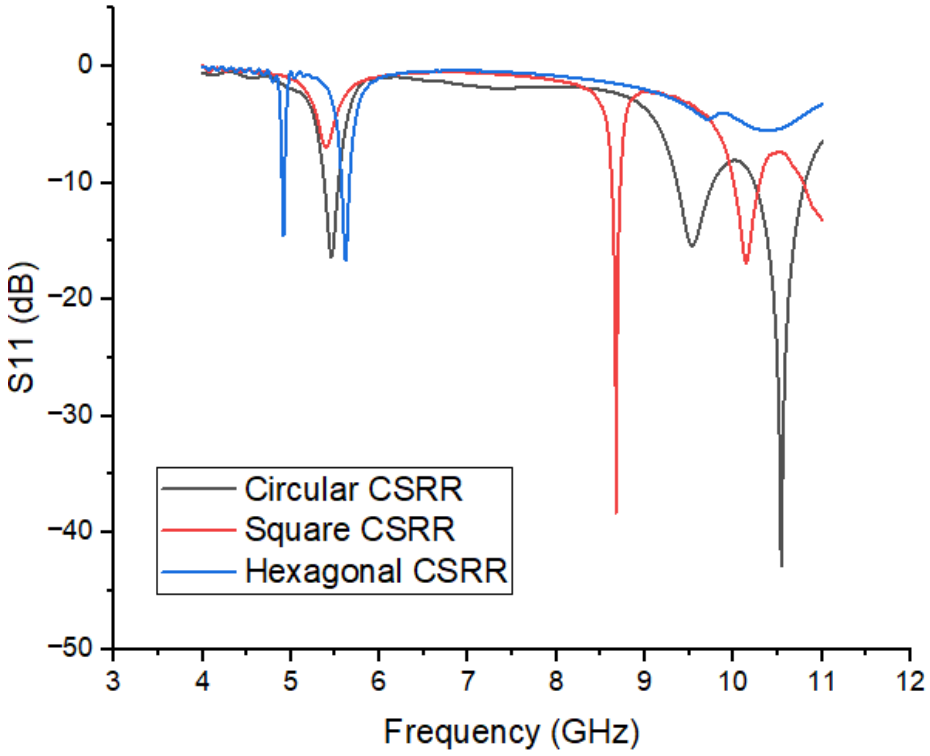

Fig. 4.12. Simulated S_{11} of the sensor at different CSRR shapes.

4.4 Determination of the Sensing Region

The analysis of the electric field distribution and surface current density of the sensor was conducted in order to identify the region with the highest sensitivity. Fig. 4.13 depicts the distribution of electric field and surface current of the sensor. The area surrounding of CSRR is associated with the localization of the most significant levels of intense electric field and surface current density. The propagation of an intense electric field will induce an interaction with the glucose sample, resulting in a modification of its dielectric characteristics, particularly relative permittivity and loss tangent. The alteration in these will result in a variation of the reflection coefficient of the sensor. Therefore, this particular location that has been selected as the designated area wherein the SUT will be positioned.

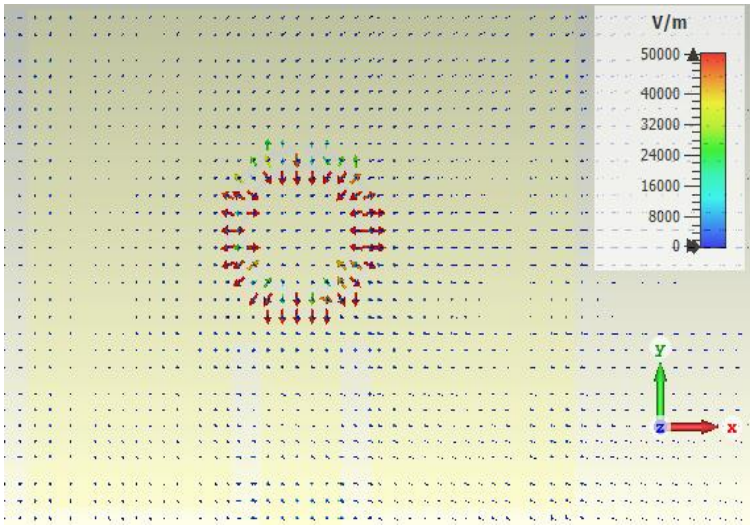

(a)

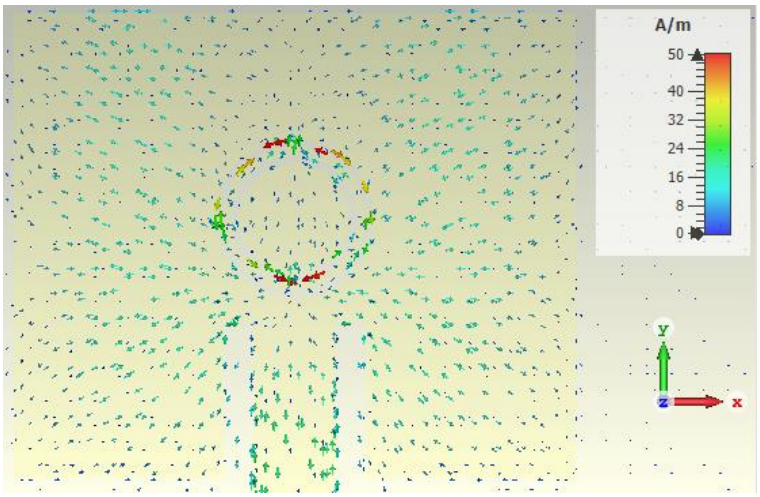

(b)

Fig. 4.13. (a) Electric field distribution (b) Surface current density of the sensor.

4.5 Gain and Radiation Efficiency of the Sensor

Fig. 4.14 (a) and Fig. 4.14 (b) show the simulated far-field 3-D and 2-D realized gain pattern of the sensor respectively at its resonant frequency that is about 10.5 GHz. The radiation at this frequency exhibits a main lobe magnitude of 6.12 dBi towards 42°. The 3-dB angular beam-width is 42.3° whereas the side lobe level is observed to be -14.7 dBi, which results the maximum power concentration along the major lobe of the sensor. The radiation efficiency of the sensor is depicted in Fig. 4.15. The sensor exhibits an impressive radiation efficiency of 0.9 i.e. 90% at 10.5 GHz.

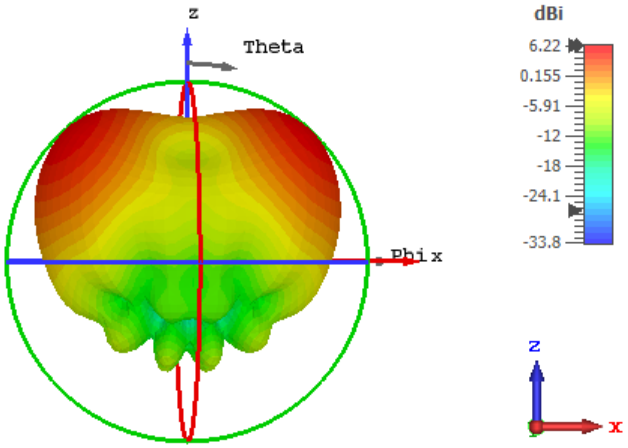

(a)

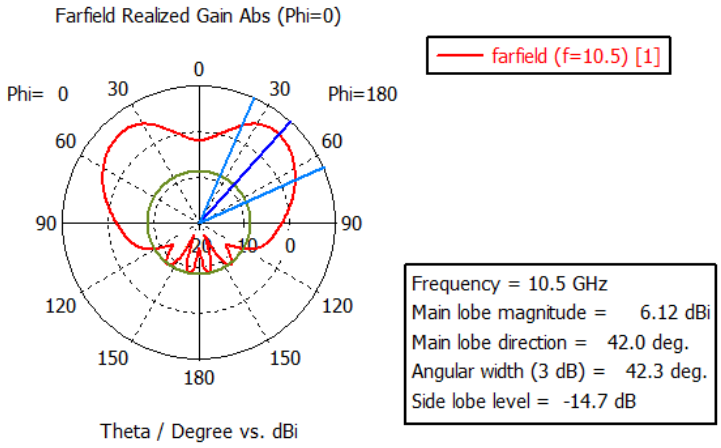

(b)

Fig. 4.14. Simulated far-field (a) 3-D and (b) 2-D realized gain pattern of the sensor.

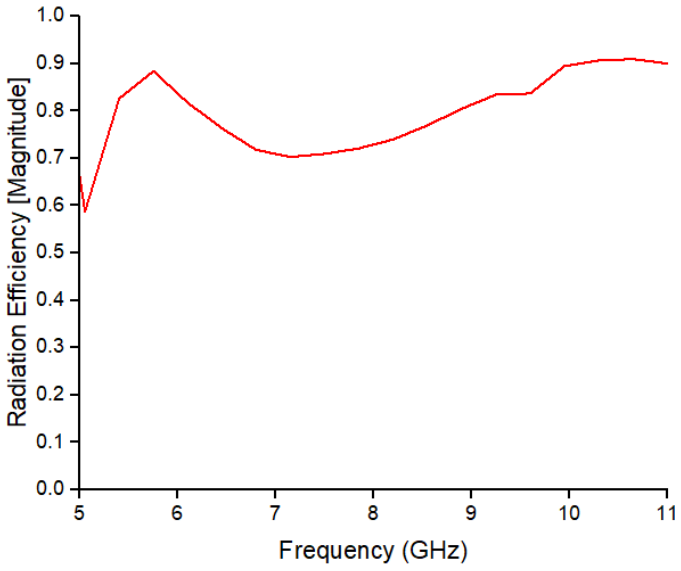

Fig. 4.15. The radiation efficiency plot of the sensor.

4.6 Analysis on Metamaterial Properties

Metamaterials refer to systematically developed materials, typically organized in periodic arrangements, which exhibit a range of distinctive properties that are not commonly observed in natural materials. The growing interest on metamaterials can be attributed to their exceptional physical attributes pertaining to sound, elasticity and electromagnetic waves. These attributes, which cannot be observed in natural materials, encompass negative refractive index, negative density, negative incremental stiffness, negative Poisson's ratio, and negative thermal conductivity [48] [49]. The extraordinary behavior exhibited by metamaterials is not dependent upon the materials that make it up, rather its characteristics are influenced by some other factors like shape, size, configuration, and alignments. Metamaterials commonly have dimensions that are comparatively smaller than the wavelength to which they are subjected; this is why they can also be called subwavelength structures. For example, a CSRR based sensor has been proposed to detect ethanol and petrol that resonates at a wavelength of λ/12 [50], and an SRR based sensor for DNA sensing has been presented that resonates at a wavelength of λ/15 [51]. Unlike natural materials, the metamaterials exhibits unexpected patterns of interaction with both light and sound waves. Therefore, their ability to control the propagation of electromagnetic wave enables them for utilization in sensor applications. The electromagnetic properties of metamaterials can be described and quantified by employing the subsequent mathematical equations [52].

$$\text{Permittivity, } \varepsilon = \frac{n}{Z} \tag{4.6}$$

$$\text{Permeability, } \mu = n \times Z \tag{4.7}$$

Here, the symbols ‘n’ and ‘Z’ represent the refractive index and impedance, respectively. These parameters can be computed using the following equations:

$$\text{Impedance, } Z = \sqrt{\frac{(1+S_{11})^2 - S_{21}{}^2}{(1-S_{11})^2 - S_{21}{}^2}} \tag{4.8}$$

$$\text{Refractive index, } n = \frac{1}{k_0 d}\left[\left\{\left(\ln\left(e^{ink_0 d}\right)\right)'' + 2m\pi\right\} - i\left(\ln\left(e^{ink_0 d}\right)\right)'\right] \tag{4.9}$$

Here, the notation $(\,)'$ and $(\,)''$ is used to represent the real and imaginary components, respectively. The variable d represents the maximum width of the metamaterial cell, m is a number that corresponds to the branch index of n', while k_0 denotes the wave number.

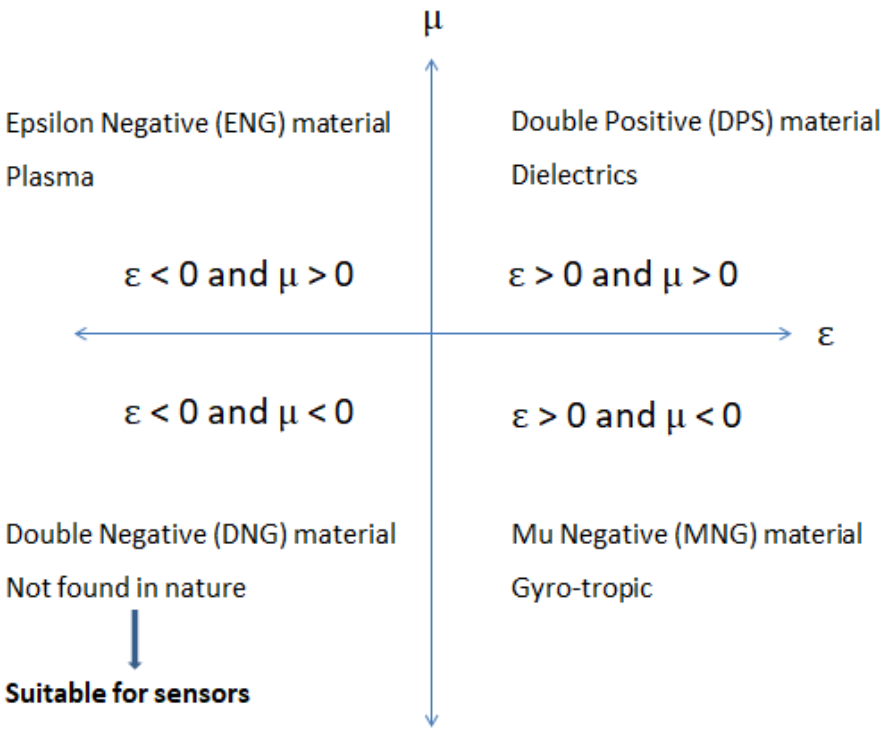

Fig. 4.16. Classification of metamaterial based on electromagnetic properties.

Metamaterials are categorized according to their electromagnetic properties i.e. permittivity (ε) and permeability (μ), as illustrated in Fig. 4.16. If both the values for ε and μ of the material are positive, it will be classified as Double Positive (DPS) and will be categorized under quadrant I. Materials with negative ε and positive μ is denoted as Epsilon Negative (ENG) and falls into quadrant II. Mu Negative (MNG) materials are located in quadrant IV, characterized by positive ε and negative μ. Materials that possess both negative permittivity and permeability are commonly referred to as Double Negative (DNG) and they belong to quadrant III [53]. Such types of materials are also known as Left Hand Materials (LHM) because the electric field $\vec{E}$, the magnetic field $\vec{H}$, and the wave vector $\vec{k}$ form a left set of vectors. According to Maxwell's equations, the refractive index of an object is expected to be negative if both its permittivity and permeability values are negative. The presence of negative refractive index in LHM material leads to the accumulation of incident electromagnetic waves which is very vital for the glucose sensing operation [54].

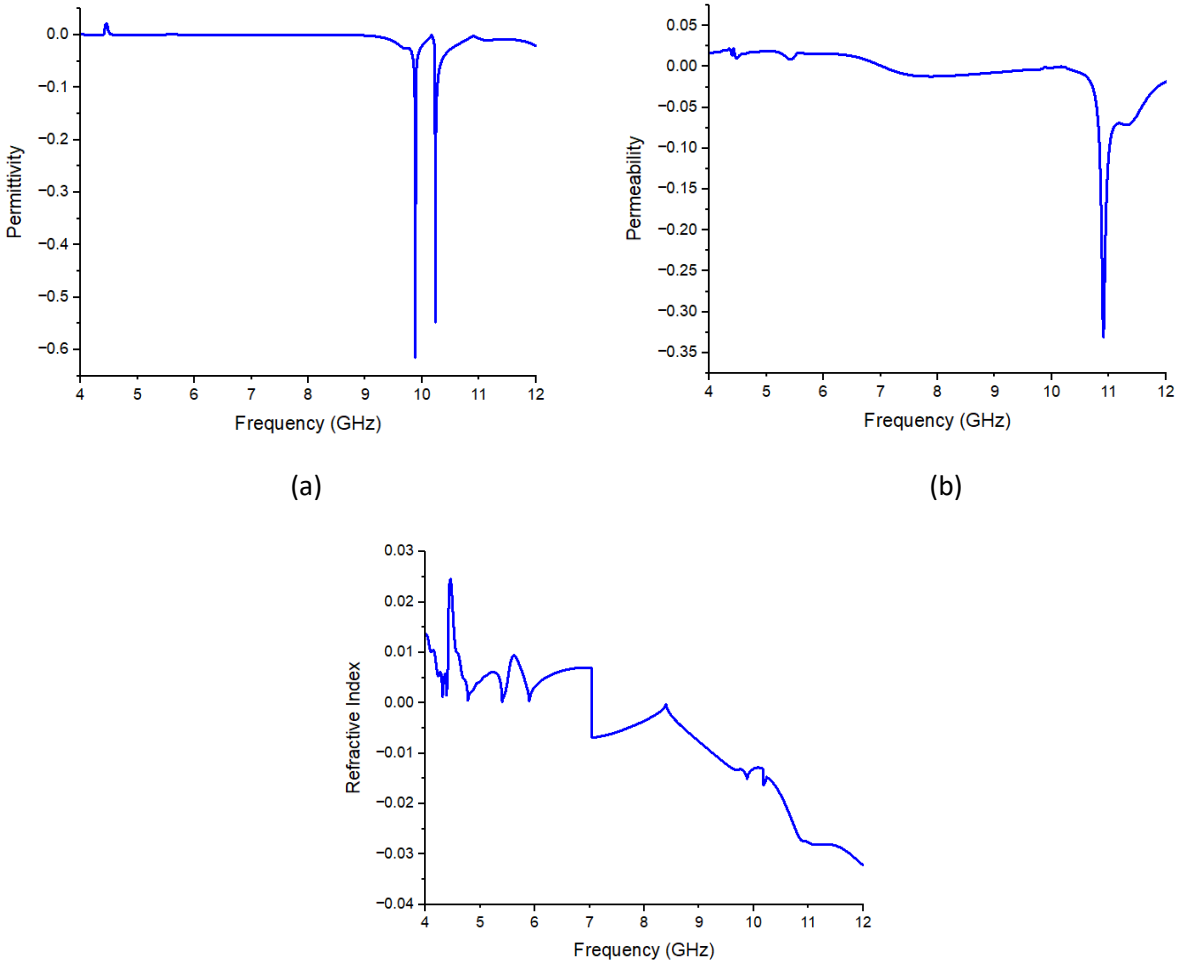

Fig. 4.17. The (a) real permittivity, (b) real permeability, (c) refractive index of the metamaterial unit cell.

The extracted metamaterial characteristics are illustrated in Fig. 4.17. The investigation reveals that the metamaterial unit cell demonstrates negative values for both permittivity and permeability while operating at the resonant frequency. The refractive index is also negative as it was assumed. Hence, the metamaterial has the potential ability to accumulate strong electric field, a critical factor in facilitating the sensing process.

CHAPTER 5

RESULTS AND DISCUSSIONS

5.1 Analysis with Aqueous Glucose Solution

The initial phase of this study entails identifying the concentration of glucose in aqueous solution. Fig. 5.1 shows the perspective view of a plexiglass container ($\varepsilon_r' = 3.9$ and tan δ = 0.001) positioned directly above the CSRR region, which is considered the most sensitive region of the sensor. A range of water glucose concentrations, spanning from 50 mg/dL to 300 mg/dL, is introduced into the container. The subsequent analysis involves evaluating the function of the antenna using these solutions.

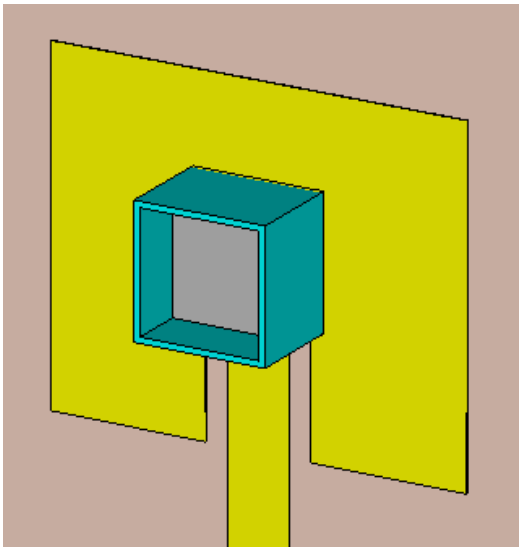

Fig. 5.1. Perspective view of the sensor with aqueous glucose solution.

The intense electric field present in the sensing region comes in interaction with the SUT, which is glucose solution in this case. The highly sensitive sensor has the ability to detect even the minute variations in the permittivity of the SUT. The amplitude of reflection coefficient of the sensor will exhibit variations in response to alterations in the concentrations of the glucose solution as depicted in Fig. 5.2. In the inset of this figure, enlarged portion of the change in reflection coefficient around the resonant frequency are shown. The figure clearly demonstrates that there is an increase in the magnitude of $|S_{11}$ (dB)| as the amount of glucose is increased. Through the examination of the variation in the amplitude of the reflection coefficient of the sensor, it is possible to ascertain the concentration of glucose in

the solution. The amplitude of reflection coefficients of the sensor, corresponding to different aqueous glucose concentrations (AGC) are presented in Table 5.1.

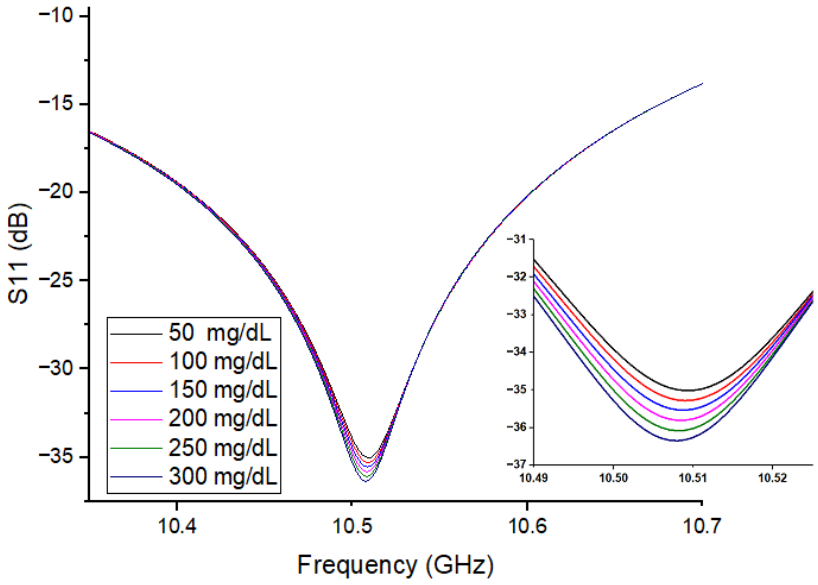

Fig. 5.2. Variation of S_{11} in dB of the sensor with varying concentrations of glucose in water solution.

Table 5.1: AGC with corresponding S_{11}

AGC (mg/dL)	**S_{11} (dB)**
50	-34.99
100	-35.26
150	-35.53
200	-35.81
250	-36.08
300	-36.35

The simple linear regression technique has been used to predict the AGC based on the acquired values of S_{11} in dB derived from Table 5.1. The regression equation can be described in the following form:

$$y = mx + b \tag{5.1}$$

Here, x denotes BGL and y denotes obtained reflection coefficient from the plot. The process of constructing the regression equation that establishes the relationship between AGC and S_{11}(dB) is outlined in Table 5.2, followed by further computations.

Table 5.2: Regression analysis to estimate AGC

x	y	$x - \bar{x}$	$y - \bar{y}$	$(x - \bar{x})^2$	$(x - \bar{x})(y - \bar{y})$
50	-34.99	-125	0.68	0.4624	-85
100	-35.26	-75	0.41	0.1681	-30.75
150	-35.53	-25	0.14	0.0196	-3.5
200	-35.81	25	-0.14	0.0196	-3.5
250	-36.08	75	-0.41	0.1681	-30.75
300	-36.35	125	-0.68	0.4624	-85
				$\sum(x-\bar{x})^2 = 43750$	$\sum(x-\bar{x})(y-\bar{y}) = -238.5$

In this context, $\bar{x} = 175$ and $\bar{y} = -35.67$ represent the average values of the variables x and y, respectively. The value of regression coefficient, *m* is computed as:

$$m = \frac{\sum(x-\bar{x})(y-\bar{y})}{\sum(x-\bar{x})^2} = 5.45\times10^{-3} \tag{5.2}$$

The value of b can be computed as:

$$\bar{y} = m\bar{x} + b$$

$$\Rightarrow \quad -35.67 = \left(-5.45\times10^{-3}\times175\right) + b$$

$$\Rightarrow \quad b = -34.72$$

The obtained regression equation can be expressed as:

$$y = -34.72 - 5.45\times10^{-3}x \tag{5.3}$$

The correlation coefficient (R^2) is employed to demonstrate the capability of the regression model to predict the given data. The process of computing correlation coefficient is described below.

Table 5.3: Determination of R^2 in the regression analysis to estimate AGC

x	y	$(y - \bar{y})^2$	$\hat{y}$	$(\hat{y} - \bar{y})$	$(\hat{y} - \bar{y})^2$
50	-34.99	0.462	-34.99	0.68	0.462
100	-35.26	0.168	-35.27	0.4	0.16
150	-35.53	0.02	-35.54	0.13	0.017
200	-35.81	0.02	-35.81	-0.14	0.02
250	-36.08	0.168	-36.08	-0.41	0.168
300	-36.35	0.462	-36.36	-0.68	0.462
		$\sum(y-\bar{y})^2$			$\sum(\hat{y}-\bar{y})^2 = 1.289$

The value of R^2 is obtained as:

$$R^2 = \frac{\sum(\hat{y}-\bar{y})^2}{\sum(y-\bar{y})^2} = 0.992 \tag{5.4}$$

In this equation, $\hat{y}$ represents the predicted value of y. The value correlation coefficient (R^2) is 0.992, which indicates a very close relationship between AGC and S_{11}. The AGC can be computed by employing the mathematical regression model. Table 5.4 presents an overview of the reference AGC and the resultant AGC values derived from the model, along with the corresponding error. The representation of the actual S_{11} (dB) and the estimated S_{11} (dB) derived from the model for glucose concentrations in aqueous solutions along with the fitted curve is plotted in Fig. 5.3. It is apparent from the plot that the real and estimated values of S_{11} are nearly identical.

Table 5.4: An overview of actual and estimated AGC

Reference AGC (mg/dL)	**Estimated AGC (mg/dL)**	**Error (%)**
50	49.54	0.92
100	99.08	0.92
150	148.62	0.92
200	200	0
250	249.54	0.184
300	299.08	0.31

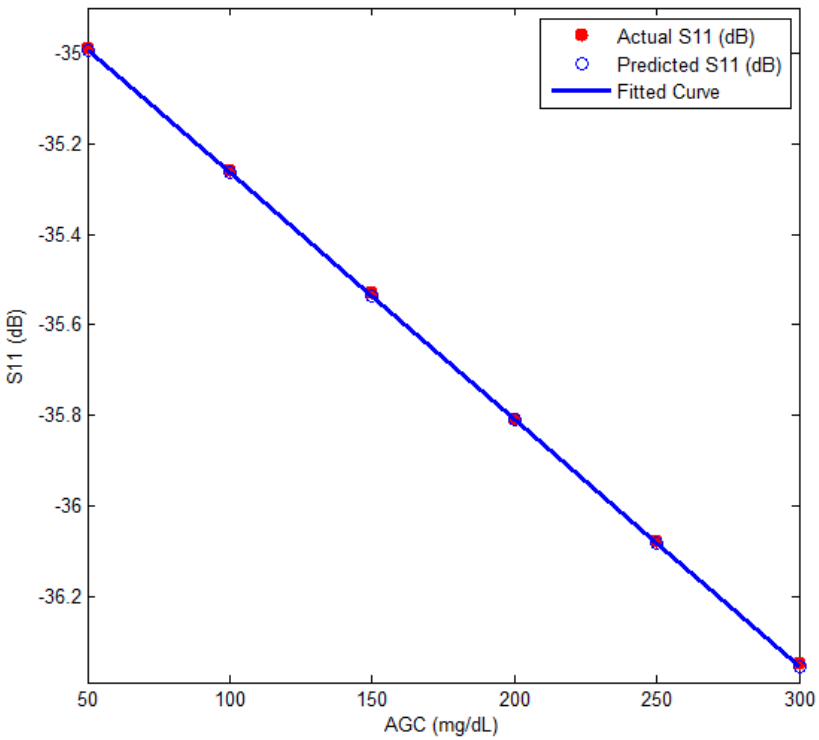

Fig. 5.3. Actual and estimated S_{11} (dB) for different AGC.

5.2 Analysis with Human Finger Model

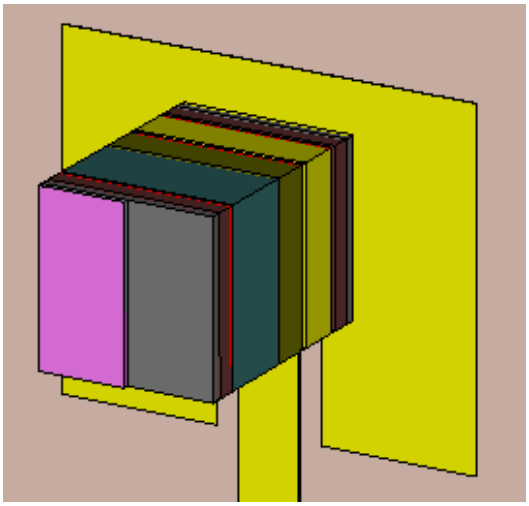

Fig. 5.4. Perspective view of the sensor with finger model placed on it.

The main objective of our study is to ascertain the BGL of a human finger model. The multi-layer finger model has been integrated into the sensor as depicted in Fig. 5.4. The electromagnetic waves emitted by the sensor will thereafter penetrate the layers of the finger and engage with the layers of blood. The sensor will identify and evaluate any change in

blood permittivity. Fig. 5.5 shows that an increase in blood permittivity leads to a corresponding rise in the amplitude of $|S_{11}$ (dB)|. Table 5.5 presents the amplitude of return loss of the sensor, corresponding to different blood glucose concentrations.

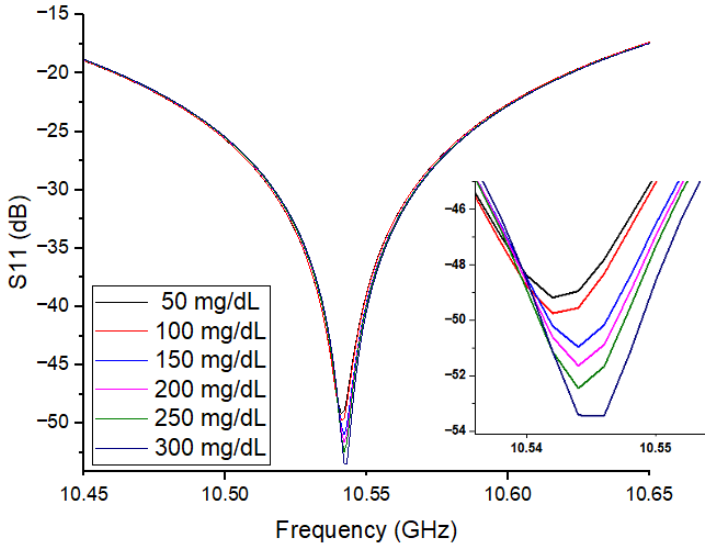

Fig. 5.5. Change in S_{11} (dB) of the sensor with different BGL.

Table 5.5: Range of BGL alongside respective S_{11} values

BGL (mg/dL)	**S_{11} (dB)**
50	-48.94
100	-49.53
150	-50.93
200	-51.64
250	-52.43
300	-53.42

The sensitivity of the sensor is calculated as the ratio of the variation in the magnitude of S_{11} associated with alterations in glucose concentration. The sensitivity is found to be 1.792 dB per (mg/mL) which indicates that the antenna exhibits a strong response even in the presence of small variations in blood glucose concentrations. Subsequently the value of sensitivity is computed as:

$$Sensitivity = \sum_{i=1}^{n-1} \frac{(s_{i+1} - s_i)}{(g_{i+1} - g_i)} \tag{5.5}$$

Here, s_i = ith value of reflection coefficient and g_i = ith value of glucose concentration. The simple linear regression technique has been used to predict the BGL based on the acquired values of S_{11} in dB derived from Table 5.5. The process of constructing the regression equation that establishes the relationship between BGL and S_{11}(dB) is outlined in Table 5.6, followed by further computations.

Table 5.6: Regression analysis to estimate BGL

x	y	$x - \bar{x}$	$y - \bar{y}$	$(x - \bar{x})^2$	$(x - \bar{x})(y - \bar{y})$
50	-48.94	-125	2.21	4.88	-276.25
100	-49.53	-75	1.62	2.62	-121.5
150	-50.93	-25	0.22	0.048	-5.5
200	-51.64	25	-0.49	0.24	-12.25
250	-52.43	75	-1.28	1.638	-96
300	-53.42	125	-2.27	5.15	-283.75
				$\sum(x-\bar{x})^2 = 43750$	$\sum(x-\bar{x})(y-\bar{y}) = -795.25$

In this context, $\bar{x} = 175$ and $\bar{y} = -51.15$ represent the average values of the variables x and y, respectively. The subsequent equation is applied to compute the value of regression coefficient, *m*:

$$m = \frac{\sum(x-\bar{x})(y-\bar{y})}{\sum(x-\bar{x})^2} = -0.018 \tag{5.6}$$

The value of b can be computed as:

$$\bar{y} = m\bar{x} + b$$

$$\Rightarrow \quad -51.15 = \left(-0.018 \times 175\right) + b$$

$$\Rightarrow \quad b = -48$$

The obtained regression equation can be expressed as:

$$y = -48 - 0.018x \tag{5.7}$$

The process of computing correlation coefficient (R^2) is narrated below.

Table 5.7: Determination of R^2 in the regression analysis to estimate BGL

x	y	$(y - \bar{y})^2$	$\hat{y}$	$(\hat{y} - \bar{y})$	$(\hat{y} - \bar{y})^2$
50	-48.94	4.88	-48.9	2.25	5.06
100	-49.53	2.62	-49.8	1.35	1.82
150	-50.93	0.05	-50.7	0.45	0.2
200	-51.64	0.24	-51.6	-0.45	0.2
250	-52.43	1.64	-52.5	-1.35	1.82
300	-53.42	5.15	-53.4	-2.25	5.06
		$\sum(y - \bar{y})^2 = 14.58$			$\sum(\hat{y} - \bar{y})^2 = 14.16$

The value of R^2 is obtained as:

$$R^2 = \frac{\sum(\hat{y} - \bar{y})^2}{\sum(y - \bar{y})^2} = 0.971 \tag{5.8}$$

The value correlation coefficient (R^2) is 0.971, implying a highly significant correlation between AGC and S_{11}. The BGL can be computed by employing the mathematical regression model. Table 5.8 presents an overview of the reference BGL and the resultant BGL values derived from the model, along with the corresponding error. The representation of the actual S_{11} (dB) and the predicted S_{11} (dB) derived from the model for different blood glucose concentrations including the fitted curve is plotted in Fig. 5.6. The actual and predicted values of S_{11} exhibit a high degree of similarity which is obvious from the plot.

Table 5.8: An overview of actual and estimated BGL

Reference BGL (mg/dL)	**Estimated BGL (mg/dL)**	**Error (%)**
50	52.22	4.44
100	85	15
150	162.78	8.52
200	202.22	1.11
250	246.11	1.56
300	301.11	0.37

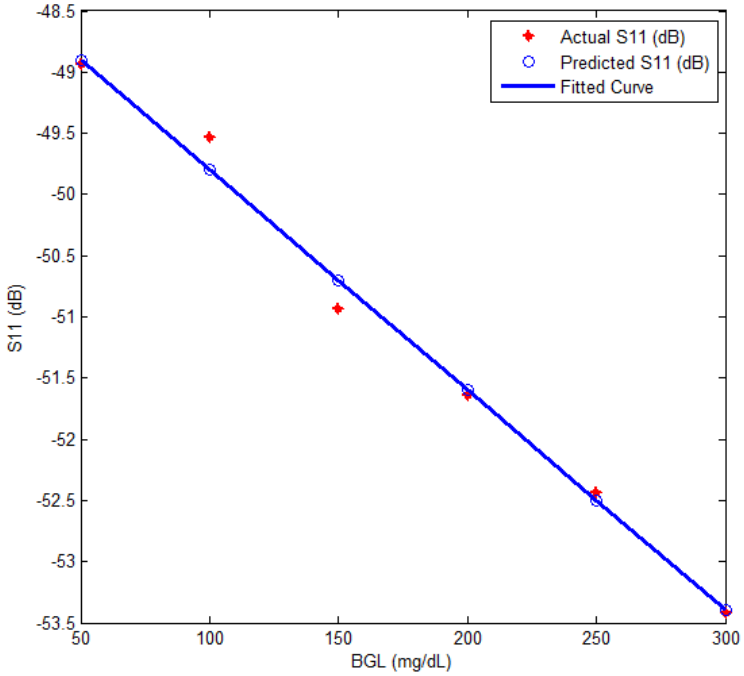

Fig. 5.6. Actual and predicted S_{11} (dB) for different BGL.

5.3 Analysis with Variation of Finger Tissues

The thickness of the finger tissues can vary among individuals, depending on factors such as body composition, gender, age, ethnicity etc. Therefore, it is necessary to do an analysis in order to comprehend the relationship between the thicknesses of finger tissues and the reflection coefficient of the sensor. The impact of varying the thickness of both dry and wet skin is demonstrated in Fig. 5.7 (a). By examining the figure, it is evident that altering the skin thickness results in modifications to both the resonant frequency and the amplitude of the reflection coefficient. Fig. 5.7 (b) illustrates the analysis involving the variation of blood layer thickness. There are slight variations in S_{11} values for blood layer thickness ranging from 0.22 mm to 0.25 mm. However, when the thickness ranges from 0.26 mm to 0.28 mm, there are significant variations in the amplitude of S_{11} of the sensor. The asymmetrical changes in resonant frequency and return loss, as depicted in Fig. 5.7 (c), are caused by variations in the thickness of fat layers. The reflection coefficient increases as the thickness of both the muscle and bone layers increases, as seen in Fig 5.7 (d) and Fig. 5.7 (e) respectively. So, enhanced thickness in muscle and bone layers will result in higher reflection. The increase in tissue thickness will result in a drop in the resonant frequency for muscle and an increase in the resonant frequency for bone. The investigation conducted on nail tissue in Fig. 5.7 (f) reveals that there is minimal alteration in both resonant frequency

and amplitude when the nail thickness is varied. So the thickness of the nail layer has minimal impact on the characteristics of the sensor. It also indicates that the radiation experiences attenuation in different finger tissues and has limited penetration into the nail layer.

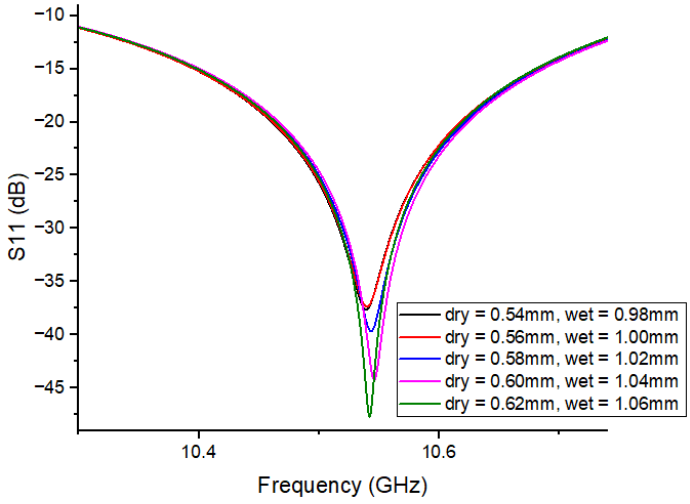

(a)

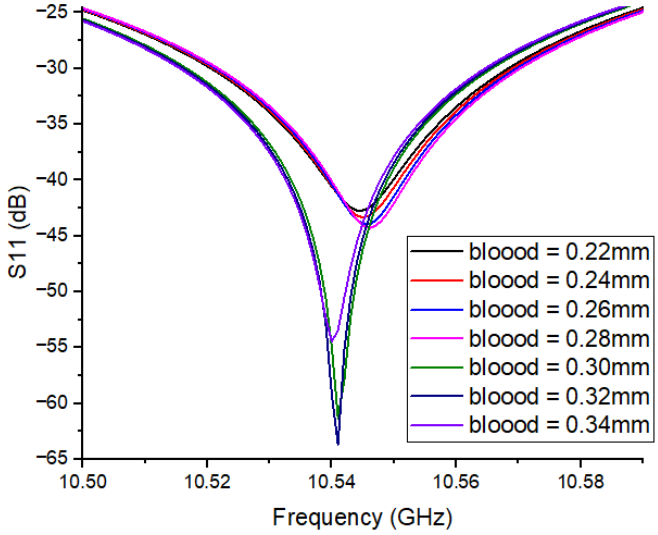

(b)

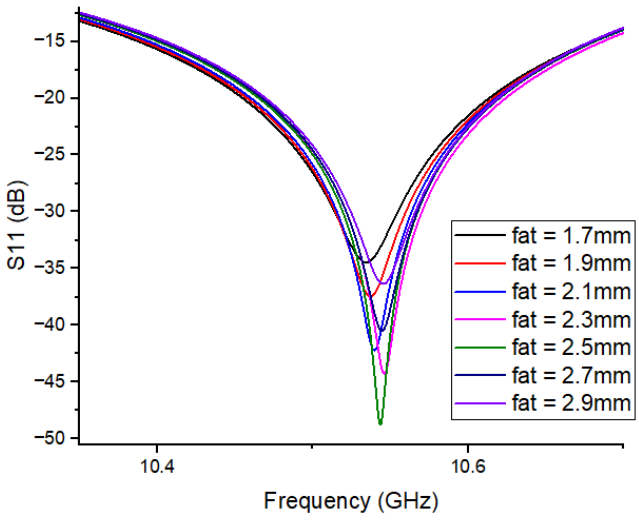
S11 (dB)
Frequency (GHz)
fat = 1.7mm
fat = 1.9mm
fat = 2.1mm
fat = 2.3mm
fat = 2.5mm
fat = 2.7mm
fat = 2.9mm

(c)

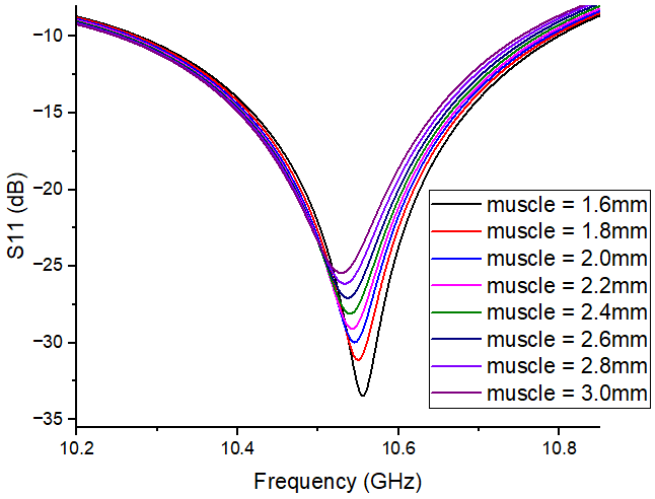
S11 (dB)
Frequency (GHz)
muscle = 1.6mm
muscle = 1.8mm
muscle = 2.0mm
muscle = 2.2mm
muscle = 2.4mm
muscle = 2.6mm
muscle = 2.8mm
muscle = 3.0mm

(d)

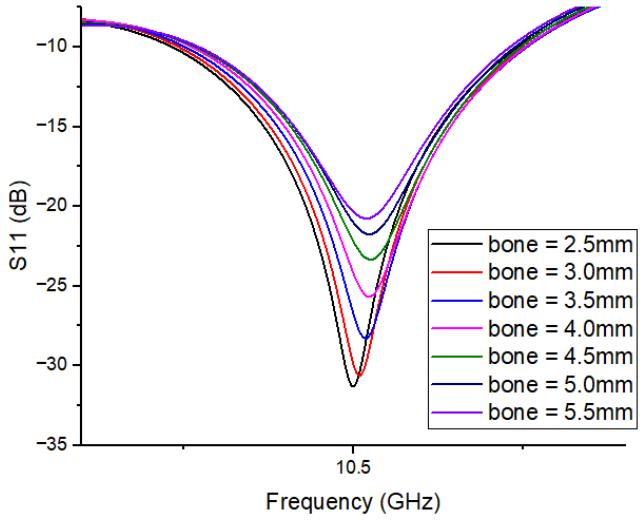
S11 (dB)
Frequency (GHz)
bone = 2.5mm
bone = 3.0mm
bone = 3.5mm
bone = 4.0mm
bone = 4.5mm
bone = 5.0mm
bone = 5.5mm

(e)

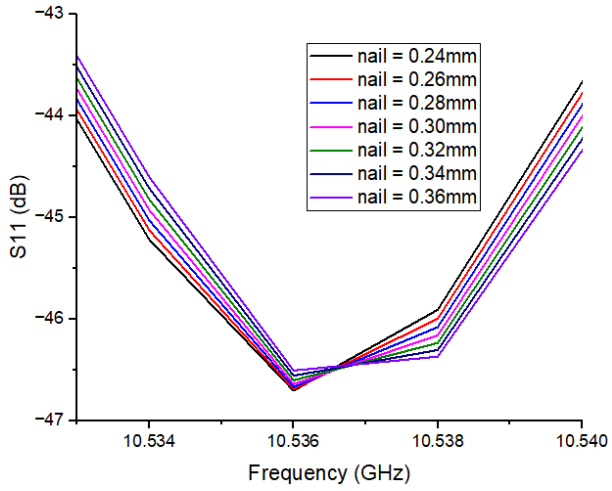

(f)

Fig. 5.7. Variation of S_{11} of the sensor with changes in thickness of (a) dry and wet skin, (b) blood, (c) fat, (d) muscle, (e) bone and (f) nail.

To summarize, the variations in tissue thickness will result in alterations in the characteristics of the sensor, thereby impacting the readings of glucose levels. Hence, the capacity to scale among diverse diabetic individuals with varying blood parameters is a challenge. This issue can be resolved by conducting a single invasive personal calibration of the sensor, in which the individual's blood glucose level will be examined invasively and then with the proposed sensor. By conducting a comparison of the two results, the sensor will be adjusted to accurately measure glucose level of a specific individual. An alternative approach might involve integrating a machine learning model trained on a diverse dataset consisting of a substantial number of individuals.

5.4 Sensor Accuracy and Safety Analysis

The Clarke Error Grid Analysis and Mean Absolute Relative Difference (MARD) are frequently utilized techniques for assessing the accuracy of glucose level detection. These analyses aid in evaluating the effectiveness of a glucose monitoring device compared to reference data. The examination of Specific Absorption Rate (SAR) is used to assess the RF safety pertaining to the human body when subjected to electromagnetic fields. SAR indicates the measure of electromagnetic energy absorption by the human body when exposed to RF electromagnetic fields. The SAR analysis offers a thorough comprehension of the absorption of RF radiation by the human body and its potential health effects. In the subsequent sections, an investigation on these methods is discussed to verify the accuracy and safety of the proposed sensor in the field of glucose level detection.

5.4.1 Accuracy Verification using MARD Analysis

MARD is a popular statistical analysis that provides a single value summarizing the overall accuracy of the glucose sensing operation. The accuracy of the proposed glucose sensor has been quantified using MARD analysis, which can be described as:

$$MARD = \frac{1}{N} \sum_{i=1}^{n} \frac{|E_i - A_i|}{A_i} \tag{5.9}$$

Here, E_i is estimated BGL and A_i is actual BGL. After substituting the values of estimated and actual BGL from Table 5.8, the value of MARD is computed to be 0.051. This indicates that there is only 5.1% fluctuation between the estimated and actual BGL.

5.4.2 Accuracy Assessment using Clarke Error Grid Analysis

The strength and direction of the correlation between predicted and reference BGL values of the proposed sensor was verified using the Clarke error grid analysis as depicted in Fig. 5.8. The grid is comprised of five distinct zones, with each zone denoting a distinct level of risk associated with the variation between estimated and reference glucose values. Zone A is commonly known as the clinically accurate zone, since it has a prediction error rate that is below 20%. The occurrence of prediction error is observed to be higher in Zone B and C. However, these errors remain within a safe range and do not typically lead to inaccurate course of treatment. The zone D and E is characterized by significant errors that may result risks to the health of patients [55]. It is obvious from the plot that all of the estimated BGL obtained from our study consistently remain within zone A, indicating a high level of performance for the sensor being presented.

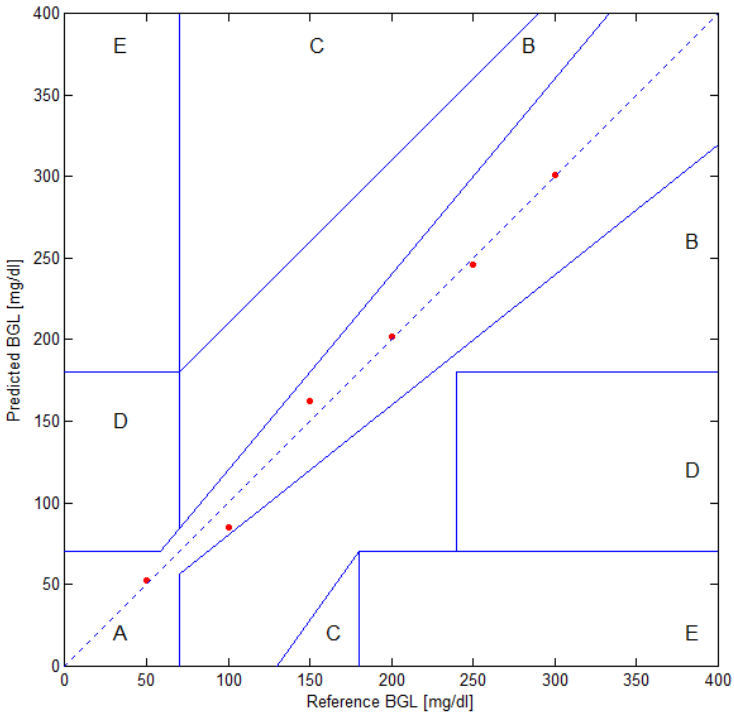

Fig. 5.8. Verification of the sensor using Clarke error grid Analysis.

5.4.3 Specific Absorption Rate (SAR) Analysis for RF Safety

In order to assess any potential risks linked to the RF electromagnetic radiation released by the glucose sensor, the SAR of the sensor is computed at its resonance frequency, which is around 10.5 GHz. The proposed human finger model has a mass of 0.52 gm. However, in order to simulate SAR distributions at 1-g, a minimum of 2 gm of finger tissue is necessary. Therefore, the thickness of each layer of the finger tissue is augmented proportionally in order to achieve a mass of about 2.2 gm. The specified power input was set to 0.5 W. The simulated SAR distribution of the proposed sensor is shown in Fig 5.9. The maximum 1-g SAR is found as 0.519 W/kg. The safety standard for SAR of 1 gm of tissue is 1.6 W/kg as recommended by IEEE C95.1-1999 [56]. Hence, the finding demonstrates that the 1-g SAR of the sensor is well below the established safety threshold, thereby posing no RF radiation hazard to the human body.

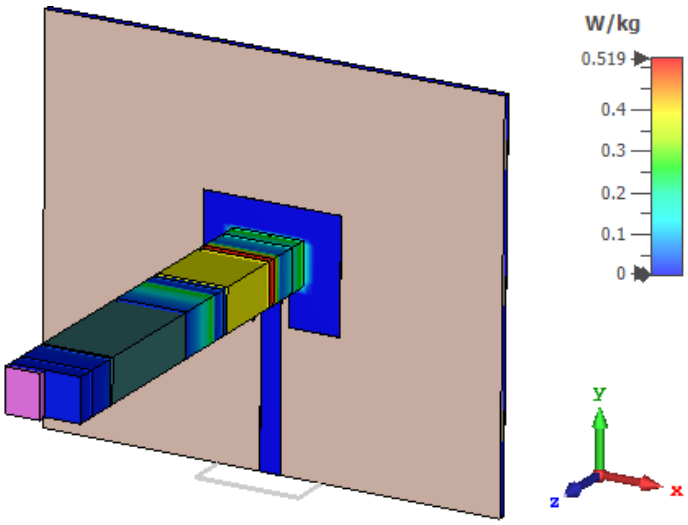

Fig. 5.9. Simulated 1-g SAR analysis of the proposed sensor at the resonant freuency.

5.5 Comparative Analysis

A comparative analysis of determining the sensitivity between the proposed sensor and other recently developed sensors is presented in Table 5.9. The highest sensitivity 1.79 dB per mg/mL, is achieved by this particular work while the sensor from the research [57] has sensitivity of 0.8 – 1 dB per mg/mL, which is the second highest among all the works. The sensitivity of other reported sensors is approximately 22 to 224 times lower than the sensitivity of the presented sensor. The enhanced sensitivity enables accurate detection of glucose levels and differentiation between small variations in glucose concentrations.

Table 5.9: Comparison with other sensors based on sensitivity

Reference	**Sensor Structure**	**Sensing parameter**	**Sensitivity (dB per mg/mL)**
[25]	Two cells of circular SRR	S_{11}	0.042
[60]	Double CSRR	S_{21}	0.008
[61]	Coplanar Single SRR	S_{11}	0.023
[62]	Chipless SRR sensor	S_{21}	0.083
[57]	Dielectric disk resonator	S_{21}	0.8 – 1
Proposed sensor	Single CSRR sensor	S_{11}	1.79

Table 5.10: Comparison based on electric field intensity

Reference	Sensor Structure	Electric Field (V/m)
[63]	Closed loop split ring sensor	1.23×10^4
[64]	Microwave planar resonator sensor	1.00×10^4
[59]	SIW with CSRR	1.91×10^3
[65]	Open stab resonator	1.13×10^4
[58]	Metamaterial based sensor	4.00×10^4
Proposed sensor	Single CSRR sensor	5.00×10^4

Table 5.10 presents another comparison based on electric field intensity. The sensor under consideration demonstrates the most intense electric field which is 5.00×10^4 V/m, leading to a strong interaction with both aqueous glucose solutions and human finger model. A metamaterial inspired sensor [58] demonstrates electric field intensity of 4.00×10^4, which aligns closely with the outcomes of this research. The lowest electric field intensity of 1.91×10^3 is attained by another CSRR based sensor incorporating SIW [59]. The proposed sensor exhibits a significant accumulation of electric field, demonstrating a high level of sensitivity and highly accurate detection capability for glucose levels. These characteristics affirm the superior performance of the proposed sensor.

CHAPTER 6

CONCLUSION

6.1 Conclusion

A biomedical sensor dedicated for glucose concentration measurement has been designed and analyzed in this research paper. A metamaterial structure, namely CSRR is integrated on the device in order to exploit its unique characteristics for improved sensing capabilities. Through the analysis of the S-parameters of the sensor, it is determined that the optimal design consists of a single cell of CSRR positioned 0.8 mm above the center of the patch. The outer ring radius of the CSRR has been specified at 3 mm, while the inner ring radius is set at 2.4 mm. Three distinct geometric shapes, namely circular, square, and hexagonal shapes, are evaluated and the circular shape is ultimately selected as the optimal choice. The CSRR region is selected as the sensing region as it exhibits the most intense electric field concentration and surface current density. The response of the sensor is analyzed to determine glucose level in both water glucose solution and a human finger model. Debye and Cole-Cole relaxation models are employed to determine the dielectric properties of various concentrations of water solution and finger tissues respectively. The return loss of the sensor has been observed to vary in conjunction with changes in glucose concentrations. Statistical regression equation has been developed which establish a correlation between glucose level with return loss. The sensor shows superior sensitivity of 1.79 dB per mg/mL, indicating its ability to recognize even the smallest variations in glucose concentration. The sensor possesses a MARD value of 0.051, which signifies that only 5.1% of the estimated values deviate from the actual values of glucose level. Based on the Clarke error grid analysis, it is found that all the predicted glucose levels fall within region A, which represents the clinically acceptable range. The highest 1-g SAR is obtained as 0.519 W/kg, which falls within the established safety threshold for human beings. This sensor is evaluated in terms of sensitivity and electric field intensity, in comparison to other contemporary glucose sensors. The comparison demonstrates that the proposed sensor outperforms other sensors in both criteria. With high accuracy, superior sensitivity and absence of any health risks, this sensor is an excellent option for detecting glucose levels in real-world applications.

6.2 Contributions of the Research

This research aims to achieve specific objectives and has made several original contributions. Some of these contributions have already been published in two prominent international conferences, while the remaining ones are currently being reviewed for potential publication in another reputed journal in the near future. The main contributions of this study are outlined as follows:

(i) An antenna sensor with a metamaterial element, specifically CSRR is designed and simulated. This microwave sensor can be utilized not just to monitor glucose level in human body but also can be employed in several other biomedical applications.

(ii) The analysis of the attributes of the CSRR is carried out in order to highlight the distinctive qualities that it possesses, which are not typically found in nature. By exploiting these unique characteristics of this metamaterial element, it can be incorporated into a variety of microwave devices for a wide range of applications.

(iii) The metamaterial based sensor is used to estimate both aqueous and blood glucose concentrations. This sensor can be fabricated and its prospective application can assist with controlling the worldwide diabetes epidemic.

6.3 Limitations of the Research

Nevertheless, it is essential to recognize the inherent limitations and difficulties that could affect the results of the study. For example, the aqueous glucose solutions are applied directly on the box without the utilization of any microfluidic channel. The possible impact on environmental conditions, such as temperature and humidity, is not taken into account; but these elements might influence the performance of the sensor. Another limitation arises from the usage of a single port for feeding, restricting the analysis solely to the values of the reflection coefficient S_{11}. Variations in body composition, gender, age ethnicity, and other variables might cause finger tissue thickness to differ from person to person. Because of these differences in tissue thickness, the sensor's properties will change, which in turn affects the accuracy of glucose level detection. Therefore, a single invasive calibration procedure can be adopted to address this matter. It is also to be mentioned that this work solely consists of simulation-based research, lacking any experimental work to validate the theory and analysis of the sensor.

6.4 Future Work

In order to address the challenges that have been identified in this research, it is crucial to put forward some recommendations and approaches in the future. A microfluidic channel can be utilized to introduce aqueous glucose solutions. An additional port can be incorporated to examine the values of the transmission coefficient S_{21}. The sensor should be fabricated in real-time and validate the experimental findings against the simulated outcomes. The synthesized sensor can be examined under different temperature and humidity conditions to rectify errors caused by these factors. In addition, an artificial intelligence (AI) model trained on a broad dataset containing a significant number of individuals can help address the problems arising from differences in tissue thickness and blood dissimilarity.

REFERENCES

[1] *IDF Diabetes Atlas*, 10th ed. International Diabetes Federation, 2021.

[2] A. Talukder and Md. Z. Hossain, "Prevalence of Diabetes Mellitus and Its Associated Factors in Bangladesh: Application of Two-level Logistic Regression Model," *Sci. Rep.*, vol. 10, no. 1, p. 10237, Jun. 2020, doi: 10.1038/s41598-020-66084-9.

[3] X. Jintao, Y. Liming, L. Yufei, L. Chunyan, and C. Han, "Noninvasive and fast measurement of blood glucose in vivo by near infrared (NIR) spectroscopy," *Spectrochim. Acta. A. Mol. Biomol. Spectrosc.*, vol. 179, pp. 250–254, May 2017, doi: 10.1016/j.saa.2017.02.032.

[4] J. Kottmann, J. M. Rey, and M. W. Sigrist, "Mid-Infrared Photoacoustic Detection of Glucose in Human Skin: Towards Non-Invasive Diagnostics.," *Sensors*, vol. 16, no. 10, Oct. 2016, doi: 10.3390/s16101663.

[5] C. Stark, R. Behroozian, B. Redmer, F. Fiedler, and S. Müller, "Real-time compensation method for robust polarimetric determination of glucose in turbid media," *Biomed. Opt. Express*, vol. 10, no. 1, pp. 308–321, Jan. 2019, doi: 10.1364/BOE.10.000308.

[6] S. P. Singh *et al.*, "Evaluation of accuracy dependence of Raman spectroscopic models on the ratio of calibration and validation points for non-invasive glucose sensing.," *Anal. Bioanal. Chem.*, vol. 410, no. 25, pp. 6469–6475, Oct. 2018, doi: 10.1007/s00216-018-1244-y.

[7] D. Yang *et al.*, "Glucose Sensing Using Surface-Enhanced Raman-Mode Constraining," *Anal. Chem.*, vol. 90, no. 24, pp. 14269–14278, Dec. 2018, doi: 10.1021/acs.analchem.8b03420.

[8] L. R. De Pretto, T. M. Yoshimura, M. S. Ribeiro, and A. Zanardi de Freitas, "Optical coherence tomography for blood glucose monitoring in vitro through spatial and temporal approaches.," *J. Biomed. Opt.*, vol. 21, no. 8, p. 86007, Aug. 2016, doi: 10.1117/1.JBO.21.8.086007.

[9] T.-L. Chen, Y.-L. Lo, C.-C. Liao, and Q.-H. Phan, "Noninvasive measurement of glucose concentration on human fingertip by optical coherence tomography.," *J. Biomed. Opt.*, vol. 23, no. 4, pp. 1–9, Apr. 2018, doi: 10.1117/1.JBO.23.4.047001.

[10] W. Zhang, Y. Du, and M. L. Wang, "Noninvasive glucose monitoring using saliva nano-biosensor," *Sens. Bio-Sens. Res.*, vol. 4, pp. 23–29, Jun. 2015, doi: 10.1016/j.sbsr.2015.02.002.

[11] D. Agustini, M. F. Bergamini, and L. H. Marcolino-Junior, "Tear glucose detection combining microfluidic thread based device, amperometric biosensor and microflow injection analysis.," *Biosens. Bioelectron.*, vol. 98, pp. 161–167, Dec. 2017, doi: 10.1016/j.bios.2017.06.035.

[12] Q. Zhai *et al.*, "Enokitake Mushroom-like Standing Gold Nanowires toward Wearable Noninvasive Bimodal Glucose and Strain Sensing," *ACS Appl. Mater. Interfaces*, vol. 11, no. 10, pp. 9724–9729, Mar. 2019, doi: 10.1021/acsami.8b19383.

[13] Y. Chen *et al.*, "Skin-like biosensor system via electrochemical channels for noninvasive blood glucose monitoring.," *Sci. Adv.*, vol. 3, no. 12, p. e1701629, Dec. 2017, doi: 10.1126/sciadv.1701629.

[14] H. Fu, X. Xiao, J. Li, and Y. Zong, "Study on a Glucose Concentration Measurement System Based on Microwave Perturbation Technique," *J. Microw. Power Electromagn. Energy*, vol. 49, no. 4, pp. 215–224, Jan. 2015, doi: 10.1080/08327823.2015.11689910.

[15] R. Kumari, P. N. Patel, and R. Yadav, "An ENG resonator-based microwave sensor for the characterization of aqueous glucose," *J. Phys. Appl. Phys.*, vol. 51, no. 7, p. 075601, Jan. 2018, doi: 10.1088/1361-6463/aaa5c5.

[16] S. Kim, J. Kim, A. Babajanyan, K. Lee, and B. Friedman, “Noncontact characterization of glucose by a waveguide microwave probe,” *Curr. Appl. Phys.*, vol. 9, no. 4, pp. 856–860, Jul. 2009, doi: 10.1016/j.cap.2008.08.007.
[17] K. Lee, A. Babajanyan, C. Kim, S. Kim, and B. Friedman, “Glucose aqueous solution sensing by a near-field microwave microprobe,” *Sens. Actuators Phys.*, vol. 148, no. 1, pp. 28–32, Nov. 2008, doi: 10.1016/j.sna.2008.06.024.
[18] S. Kiani, P. Rezaei, M. Karami, and R. A. Sadeghzadeh, “Band-stop filter sensor based on SIW cavity for the non-invasive measuring of blood glucose,” *IET Wirel. Sens. Syst.*, vol. 9, no. 1, pp. 1-5(4), Feb. 2019.
[19] A. A. Mohd Bahar, Z. Zakaria, M. K. Md. Arshad, A. A. M. Isa, Y. Dasril, and R. A. Alahnomi, “Real Time Microwave Biochemical Sensor Based on Circular SIW Approach for Aqueous Dielectric Detection,” *Sci. Rep.*, vol. 9, no. 1, p. 5467, Apr. 2019, doi: 10.1038/s41598-019-41702-3.
[20] A. Kandwal *et al.*, “Surface Plasmonic Feature Microwave Sensor With Highly Confined Fields for Aqueous-Glucose and Blood-Glucose Measurements,” *IEEE Trans. Instrum. Meas.*, vol. 70, pp. 1–9, 2021, doi: 10.1109/TIM.2020.3017038.
[21] V. V. Deshmukh and S. S. Chorage, “Microstrip Antennas used for Noninvasive Determination of Blood Glucose Level,” in *2020 4th International Conference on Intelligent Computing and Control Systems (ICICCS)*, May 2020, pp. 720–725. doi: 10.1109/ICICCS48265.2020.9120873.
[22] G. Govind and M. J. Akhtar, “Design of an ELC resonator-based reusable RF microfluidic sensor for blood glucose estimation,” *Sci. Rep.*, vol. 10, no. 1, p. 18842, Nov. 2020, doi: 10.1038/s41598-020-75716-z.
[23] Z. Abedeen and P. Agarwal, “Microwave sensing technique based label-free and real-time planar glucose analyzer fabricated on FR4,” *Sens. Actuators Phys.*, vol. 279, pp. 132–139, Aug. 2018, doi: 10.1016/j.sna.2018.06.011.
[24] C. Jang, J.-K. Park, H.-J. Lee, G.-H. Yun, and J.-G. Yook, “Temperature-Corrected Fluidic Glucose Sensor Based on Microwave Resonator,” *Sensors*, vol. 18, no. 11, 2018, doi: 10.3390/s18113850.
[25] M. A. Zidane, A. Rouane, C. Hamouda, and H. Amar, “Hyper-sensitive microwave sensor based on split ring resonator (SRR) for glucose measurement in water,” *Sens. Actuators Phys.*, vol. 321, p. 112601, Apr. 2021, doi: 10.1016/j.sna.2021.112601.
[26] C. G. Juan, E. Bronchalo, B. Potelon, C. Quendo, E. Ávila-Navarro, and J. M. Sabater-Navarro, “Concentration Measurement of Microliter-Volume Water–Glucose Solutions Using Q Factor of Microwave Sensors,” *IEEE Trans. Instrum. Meas.*, vol. 68, no. 7, pp. 2621–2634, Jul. 2019, doi: 10.1109/TIM.2018.2866743.
[27] X. He, X. Hao, S. Yan, F. Wu, and J. Jiang, “Biosensing using an asymmetric split-ring resonator at microwave frequency,” *Integr. Ferroelectr.*, vol. 172, no. 1, pp. 142–146, Jun. 2016, doi: 10.1080/10584587.2016.1176827.
[28] S. Zeising *et al.*, “Towards Realisation of a Non-Invasive Blood Glucose Sensor Using Microstripline,” in *2020 IEEE International Instrumentation and Measurement Technology Conference (I2MTC)*, May 2020, pp. 1–6. doi: 10.1109/I2MTC43012.2020.9128373.
[29] P. Debye, *Polar Molecules*. Dover, New York: Dover Publications, 1945.
[30] K. S. Cole and R. H. Cole, “Dispersion and Absorption in Dielectrics I. Alternating Current Characteristics,” *J. Chem. Phys.*, vol. 9, no. 4, pp. 341–351, doi: 10.1063/1.1750906.
[31] M. Hofmann, F. Trenz, R. Weigel, G. Fischer, and D. Kissinger, “A microwave sensing system for aqueous concentration measurements based on a microwave reflectometer,”

in *2012 IEEE/MTT-S International Microwave Symposium Digest*, Jun. 2012, pp. 1–3. doi: 10.1109/MWSYM.2012.6259771.
[32] M. Shokrekhodaei, D. P. Cistola, R. C. Roberts, and S. Quinones, "Non-Invasive Glucose Monitoring Using Optical Sensor and Machine Learning Techniques for Diabetes Applications," *IEEE Access*, vol. 9, pp. 73029–73045, 2021, doi: 10.1109/ACCESS.2021.3079182.
[33] A. Gorst, K. Zavyalova, V. Yakubov, A. Mironchev, and A. Zapasnoy, "Theoretical Simulation of the Near-Field Probe for Non-Invasive Measurements on Planar Layers with Biological Characteristics," *Bioengineering*, vol. 7, no. 4, 2020, doi: 10.3390/bioengineering7040149.
[34] A. Nella, R. Aldhaheri, J. Babu, and N. Sobahi, "A non-invasive method of glucose monitoring using FR4 material based microwave antenna sensor," *Sci. Eng. Compos. Mater.*, vol. 30, Apr. 2023, doi: 10.1515/secm-2022-0187.
[35] M. C. Cebedio, L. A. Rabioglio, I. E. Gelosi, R. A. Ribas, A. J. Uriz, and J. C. Moreira, "Analysis and Design of a Microwave Coplanar Sensor for Non-Invasive Blood Glucose Measurements," *IEEE Sens. J.*, vol. 20, no. 18, pp. 10572–10581, Sep. 2020, doi: 10.1109/JSEN.2020.2993182.
[36] A. Gorst, K. Zavyalova, and A. Mironchev, "Non-Invasive Determination of Glucose Concentration Using a Near-Field Sensor.," *Biosensors*, vol. 11, no. 3, Feb. 2021, doi: 10.3390/bios11030062.
[37] A. C. Metaxas and R. J. Meredith, *Industrial Microwave Heating*, vol. 1. IET, 1983.
[38] T. Yilmaz, R. Foster, and Y. Hao, "Radio-Frequency and Microwave Techniques for Non-Invasive Measurement of Blood Glucose Levels," *Diagnostics*, vol. 9, no. 1, 2019, doi: 10.3390/diagnostics9010006.
[39] S Gabriel, R W Lau, and C Gabriel, "The dielectric properties of biological tissues: III. Parametric models for the dielectric spectrum of tissues," *Phys. Med. Biol.*, vol. 41, no. 11, p. 2271, Nov. 1996, doi: 10.1088/0031-9155/41/11/003.
[40] M. N. Hasan, S. Tamanna, P. Singh, M. D. Nadeem, and M. Rudramuni, "Cylindrical Dielectric Resonator Antenna Sensor for Non-Invasive Glucose Sensing Application," in *2019 6th International Conference on Signal Processing and Integrated Networks (SPIN)*, Mar. 2019, pp. 961–964. doi: 10.1109/SPIN.2019.8711633.
[41] T. Karacolak, E. C. Moreland, and E. Topsakal, "Cole–cole model for glucose-dependent dielectric properties of blood plasma for continuous glucose monitoring," *Microw. Opt. Technol. Lett.*, vol. 55, no. 5, pp. 1160–1164, May 2013, doi: 10.1002/mop.27515.
[42] C. A. Balanis, *Antenna Theory: Analysis and Design*, 4th ed. John Wiley & Sons Inc., Hoboken, New Jersey, 2016.
[43] A. Salim and S. Lim, "Review of Recent Metamaterial Microfluidic Sensors," *Sensors*, vol. 18, p. 232, Jan. 2018, doi: 10.3390/s18010232.
[44] S. Goswami, K. Sarmah, A. Sarma, K. Sarma, and S. Baruah, "Design Considerations Pertaining to the Application of Complementary Split Ring Resonators in Microstrip Antennas," 2018. doi: 10.4018/978-1-5225-7539-9.
[45] A. E. Omer *et al.*, "Non-Invasive Real-Time Monitoring of Glucose Level Using Novel Microwave Biosensor Based on Triple-Pole CSRR," *IEEE Trans. Biomed. Circuits Syst.*, vol. 14, no. 6, pp. 1407–1420, Dec. 2020, doi: 10.1109/TBCAS.2020.3038589.
[46] A. Ebrahimi, J. Scott, and K. Ghorbani, "Microwave reflective biosensor for glucose level detection in aqueous solutions," *Sens. Actuators Phys.*, vol. 301, p. 111662, 2020.
[47] A. E. Omer *et al.*, "Low-cost portable microwave sensor for non-invasive monitoring of blood glucose level: novel design utilizing a four-cell CSRR hexagonal configuration," *Sci. Rep.*, vol. 10, no. 1, p. 15200, Sep. 2020, doi: 10.1038/s41598-020-72114-3.

[48] J. Shi and A. H. Akbarzadeh, "3D Hierarchical lattice ferroelectric metamaterials," *Int. J. Eng. Sci.*, vol. 149, p. 103247, Apr. 2020, doi: 10.1016/j.ijengsci.2020.103247.
[49] A. Arjunan, M. Singh, A. Baroutaji, and C. Wang, "Additively manufactured AlSi10Mg inherently stable thin and thick-walled lattice with negative Poisson's ratio," *Compos. Struct.*, vol. 247, p. 112469, Sep. 2020, doi: 10.1016/j.compstruct.2020.112469.
[50] V. Rawat, S. Dhobale, and S. N. Kale, "Ultra-fast selective sensing of ethanol and petrol using microwave-range metamaterial complementary split-ring resonators," *J. Appl. Phys.*, vol. 116, no. 16, p. 164106, Oct. 2014, doi: 10.1063/1.4900438.
[51] H.-J. Lee, H.-S. Lee, K.-H. Yoo, and J.-G. Yook, "DNA sensing using split-ring resonator alone at microwave regime," *J. Appl. Phys.*, vol. 108, no. 1, p. 014908, Jul. 2010, doi: 10.1063/1.3459877.
[52] X. Chen, T. M. Grzegorczyk, B.-I. Wu, J. Pacheco, and J. A. Kong, "Robust method to retrieve the constitutive effective parameters of metamaterials," *Phys. Rev. E*, vol. 70, no. 1, p. 016608, Jul. 2004, doi: 10.1103/PhysRevE.70.016608.
[53] M. Pallavi, P. Kumar, T. Ali, and S. B. Shenoy, "Modeling of a Negative Refractive Index Metamaterial Unit-Cell and Array for Aircraft Surveillance Applications," *IEEE Access*, vol. 10, pp. 99790–99812, 2022, doi: 10.1109/ACCESS.2022.3206358.
[54] Z. Jakšić, S. Vuković, J. Matovic, and D. Tanasković, "Negative Refractive Index Metasurfaces for Enhanced Biosensing.," *Mater. Basel Switz.*, vol. 4, no. 1, pp. 1–36, Dec. 2010, doi: 10.3390/ma4010001.
[55] W. L. Clarke, C. DC, L. Gonder-Frederick, W. Carter, and S. L. Pohl, "Evaluating Clinical Accuracy of Systems for Self-Monitoring of Blood Glucose," *Diabetes Care*, vol. 10, pp. 622–8, Sep. 1987, doi: 10.2337/diacare.10.5.622.
[56] "IEEE Standard for Safety Levels with Respect to Human Exposure to Radio Frequency Electromagnetic Fields, 3 kHz to 300 GHz," *IEEE Std C951-2005 Revis. IEEE Std C951-1991*, pp. 1–238, Apr. 2006, doi: 10.1109/IEEESTD.2006.99501.
[57] A. E. Omer, S. Gigoyan, G. Shaker, and S. Safavi-Naeini, "WGM-Based Sensing of Characterized Glucose- Aqueous Solutions at mm-Waves," *IEEE Access*, vol. 8, pp. 38809–38825, 2020, doi: 10.1109/ACCESS.2020.2975805.
[58] S. Kayal, T. Shaw, and D. Mitra, "Design of metamaterial-based compact and highly sensitive microwave liquid sensor," *Appl. Phys. A*, vol. 126, no. 1, p. 13, Dec. 2019, doi: 10.1007/s00339-019-3186-4.
[59] L.-C. Fan *et al.*, "A high-Q active substrate integrated waveguide based sensor for fully characterizing magneto-dielectric (MD) materials," *Sens. Actuators Phys.*, vol. 301, p. 111778, Jan. 2020, doi: 10.1016/j.sna.2019.111778.
[60] C. Jang, J. -K. Park, H. -J. Lee, G. -H. Yun, and J. -G. Yook, "Non-Invasive Fluidic Glucose Detection Based on Dual Microwave Complementary Split Ring Resonators With a Switching Circuit for Environmental Effect Elimination," *IEEE Sens. J.*, vol. 20, no. 15, pp. 8520–8527, Aug. 2020, doi: 10.1109/JSEN.2020.2984779.
[61] S. Mohammadi *et al.*, "Gold Coplanar Waveguide Resonator Integrated With a Microfluidic Channel for Aqueous Dielectric Detection," *IEEE Sens. J.*, vol. 20, no. 17, pp. 9825–9833, Sep. 2020, doi: 10.1109/JSEN.2020.2991349.
[62] M. Baghelani, Z. Abbasi, M. Daneshmand, and P. E. Light, "Non-invasive continuous-time glucose monitoring system using a chipless printable sensor based on split ring microwave resonators," *Sci. Rep.*, vol. 10, no. 1, p. 12980, Jul. 2020, doi: 10.1038/s41598-020-69547-1.
[63] A. Kandwal *et al.*, "Highly Sensitive Closed Loop Enclosed Split Ring Biosensor With High Field Confinement for Aqueous and Blood-Glucose Measurements," *Sci. Rep.*, vol. 10, no. 1, p. 4081, Mar. 2020, doi: 10.1038/s41598-020-60806-9.

[64] S. Mohammadi, A. V. Nadaraja, D. J. Roberts, and M. H. Zarifi, “Real-time and hazard-free water quality monitoring based on microwave planar resonator sensor,” *Sens. Actuators Phys.*, vol. 303, p. 111663, Mar. 2020, doi: 10.1016/j.sna.2019.111663.
[65] R. Moolat, M. Mani, S. V. Abdulrahiman, A. Pradeep, V. Kesavath, and M. Pezholil, “Liquid Permittivity Sensing Using Planar Open Stub Resonator,” *J. Electron. Mater.*, vol. 49, no. 3, pp. 2110–2117, Mar. 2020, doi: 10.1007/s11664-019-07910-3.

LIST OF PUBLICATIONS

Conference Paper

(i) M. M. Aminuzzaman and M. Hossam-E-Haider, "A Novel Non-Invasive Method to Measure Glucose Concentration Using Triple Pole CSRR Based Sensor," in *2022 12th International Conference on Electrical and Computer Engineering (ICECE)*, Dec. 2022, pp. 16–19. doi: 10.1109/ICECE57408.2022.10088604.

(ii) M. M. Aminuzzaman and M. Hossam-E-Haider, "Non-Invasive Glucose Concentration Measurement Using a Metamaterial Based Biosensor," in *2023 International Conference on Information and Communication Technology for Sustainable Development (ICICT4SD)*, Sep. 2023, pp. 21–25. doi: 10.1109/ICICT4SD59951.2023.10303308.

Journal Paper

(i) M. M. Aminuzzaman and M. Hossam-E-Haider, "Design and Analysis of a Metamaterial Based Biosensor to Determine Blood Glucose Concentration," *International Journal of Electrical and Computer Engineering (IJECE)*, (Accepted).

APPENDIX - A

MATLAB CODES

A.1 Construction of the Clarke Error Grid

```
function [total, percentage] = clarke(y,yp)
% CLARKE    Performs Clarke Error Grid Analysis

% [total, percentage] = clarke(y,yp)
%
% INPUTS:
% y             Reference values (mg/dl)
% yp            Predicted/estimtated values (mg/dl)

if nargin == 0
 error('clarke:Inputs','There are no inputs.')
end
if length(yp) ~= length(y)
    error('clarke:Inputs','Vectors y and yp must be the same length.')
end
if (max(y) > 400) || (max(yp) > 400) || (min(y) < 0) || (min(yp) < 0)
    error('clarke:Inputs','Vectors y and yp are not in the physiological
range of glucose (<400mg/dl).')
end
% ------------------------- Print figure flag ---------------------------
-----
PRINT_FIGURE = true;
% ------------------------- Determine data length -----------------------
-----
n = length(y);
% ------------------------- Plot Clarke's Error Grid --------------------
-----
h = figure;
plot(y,yp,'ko','MarkerSize',4,'MarkerFaceColor','r','MarkerEdgeColor','r');
xlabel('Reference BGL [mg/dl]');
ylabel ('Predicted BGL [mg/dl]');
title('Clarke''s Error Grid Analysis');
set(gca,'XLim',[0 400]);
set(gca,'YLim',[0 400]);
axis square
hold on
plot([0 400],[0 400],'b:')                  % Theoretical 45° regression
line
plot([0 175/3],[70 70],'b-')
% plot([175/3 320],[70 400],'k-')
plot([175/3 400/1.2],[70 400],'b-')         % replace 320 with 400/1.2
because 100*(400 - 400/1.2)/(400/1.2) =  20% error
plot([70 70],[84 400],'b-')
plot([0 70],[180 180],'b-')
plot([70 290],[180 400],'b-')               % Corrected upper B-C boundary
% plot([70 70],[0 175/3],'k-')
plot([70 70],[0 56],'b-')                   % replace 175.3 with 56 because
100*abs(56-70)/70) = 20% error
% plot([70 400],[175/3 320],'k-')
```

```
plot([70 400],[56 320],'b-')
plot([180 180],[0 70],'b-')
plot([180 400],[70 70],'b-')
plot([240 240],[70 180],'b-')
plot([240 400],[180 180],'b-')
plot([130 180],[0 70],'b-')                    % Lower B-C boundary slope OK
text(30,20,'A','FontSize',12);
text(30,150,'D','FontSize',12);
text(30,380,'E','FontSize',12);
text(150,380,'C','FontSize',12);
text(160,20,'C','FontSize',12);
text(380,20,'E','FontSize',12);
text(380,120,'D','FontSize',12);
text(380,260,'B','FontSize',12);
text(280,380,'B','FontSize',12);
set(h, 'color', 'white');                      % sets the color to white
% Specify window units
set(h, 'units', 'inches')
% Change figure and paper size (Fixed to 3x3 in)
set(h, 'Position', [0.1 0.1 3 3])
set(h, 'PaperPosition', [0.1 0.1 3 3])
if PRINT_FIGURE
    % Saves plot as a Enhanced MetaFile
    print(h,'-dmeta','Clarke_EGA');
    % Saves plot as PNG at 300 dpi
    print(h, '-dpng', 'Clarke_EGA', '-r300');
end
total = zeros(5,1);                            % Initializes output
% ------------------------------ Statistics ------------------------------
-----
for i=1:n,
    if (yp(i) <= 70 && y(i) <= 70) || (yp(i) <= 1.2*y(i) && yp(i) >=
0.8*y(i))
        total(1) = total(1) + 1;               % Zone A
    else
        if ( (y(i) >= 180) && (yp(i) <= 70) ) || ( (y(i) <= 70) && yp(i) >=
180 )
            total(5) = total(5) + 1;           % Zone E
        else
            if ((y(i) >= 70 && y(i) <= 290) && (yp(i) >= y(i) + 110) ) ||
((y(i) >= 130 && y(i) <= 180)&& (yp(i) <= (7/5)*y(i) - 182))
                total(3) = total(3) + 1;       % Zone C
            else
                if ((y(i) >= 240) && ((yp(i) >= 70) && (yp(i) <= 180))) ||
(y(i) <= 175/3 && (yp(i) <= 180) && (yp(i) >= 70)) || ((y(i) >= 175/3 &&
y(i) <= 70) && (yp(i) >= (6/5)*y(i)))
                    total(4) = total(4) + 1;% Zone D
                else
                    total(2) = total(2) + 1;% Zone B
                end                            % End of 4th if
            end                                % End of 3rd if
        end                                    % End of 2nd if
    end                                        % End of 1st if
end                                            % End of for loop
percentage = (total./n)*100;
% EOF
```

A.2 Determination of Dielectric Properties of Aqueous Glucose Concentration

```
clc;
clear all;
close all;
wt = input('Enter the value of aqueous glucose concentration: ');
f = 10.54*10^9;
eps_inf = 5.38+((30*10^-3)*wt) ;
eps_stat = 80.68-((0.207*10^-3)*wt);
tau = (9.68+((0.23*10^-3)*wt))*(10^-12);
omega_tau = 2*pi*f*tau;

eps_real = eps_inf + (eps_stat - eps_inf) / (1+(omega_tau^2))
eps_imag = ((eps_stat - eps_inf)* omega_tau)/ (1+(omega_tau^2));

tan_delta2 = eps_imag/eps_real;
```

A.3 Determination of Dielectric Properties of Blood Glucose Concentration

```
clc;
clear all;
close all;
wt = input('Enter the value of blood glucose level: ');
f = 10.54*10^9;
eps_inf = (0.0099*(wt^2))+(0.047*wt)+2.3;
eps_delta = (-0.0093*(wt^2))+(-0.21*wt)+71;
tau_ps = (0.0012*(wt^2))+(0.23*wt)+8.7;
tau = tau_ps*(10^-12);
sigma = (0.0063*(wt^2))+(-0.14*wt)+2;
omega_tau = 2*pi*f*tau;
alpha = 0.1;
epsilon_not = 8.854*10^-12;

eps = eps_inf + (eps_delta / (1+(omega_tau^(1-
alpha))))+(sigma/(2*pi*f*epsilon_not));

eps_real = eps_inf + (eps_delta * (1+(omega_tau^(1-alpha)*
sin(alpha*pi/2))))/(1+(2*omega_tau^(1-alpha)*
sin(alpha*pi/2))+(omega_tau^(2*(1-alpha))));

eps_imag = (eps_delta*omega_tau^(1-
alpha)*cos(alpha*pi/2))/(1+(2*(omega_tau^(1-alpha))*
sin(alpha*pi/2))+(omega_tau^(2*(1-alpha))));

tan_delta = eps_imag/eps_real;
```

A.4 Determination of Dielectric Properties of Finger Tissues

```
clc;
clear all;
close all;

f = 10.54*10^9;

% Dry skin

eps_inf = 4;
eps_delta = 32;
tau_ps = 7.23;
tau = 7.23*(10^-12);
sigma = 0.002;
omega_tau = 2*pi*f*tau;
alpha = 0;
epsilon_not = 8.854*10^-12;

eps_dryskin = eps_inf + (eps_delta / (1+(omega_tau^(1-
alpha))))+(sigma/(2*pi*f*epsilon_not));
eps_real_dryskin = eps_inf + (eps_delta * (1+(omega_tau^(1-alpha)*
sin(alpha*pi/2))))/(1+(2*omega_tau^(1-alpha)*
sin(alpha*pi/2))+(omega_tau^(2*(1-alpha))))
eps_imag_dryskin = (eps_delta*omega_tau^(1-
alpha)*cos(alpha*pi/2))/(1+(2*(omega_tau^(1-alpha))*
sin(alpha*pi/2))+(omega_tau^(2*(1-alpha))));

tan_delta_dryskin = eps_imag_dryskin/eps_real_dryskin;

% Wet skin

eps_inf = 4;
eps_delta = 39;
tau_ps = 7.96;
tau = 7.96*(10^-12);
sigma = 0.004;
omega_tau = 2*pi*f*tau;
alpha = 0.1;
epsilon_not = 8.854*10^-12;

eps_wetskin = eps_inf + (eps_delta / (1+(omega_tau^(1-
alpha))))+(sigma/(2*pi*f*epsilon_not));
eps_real_wetskin = eps_inf + (eps_delta * (1+(omega_tau^(1-alpha)*
sin(alpha*pi/2))))/(1+(2*omega_tau^(1-alpha)*
sin(alpha*pi/2))+(omega_tau^(2*(1-alpha))))
eps_imag_wetskin = (eps_delta*omega_tau^(1-
alpha)*cos(alpha*pi/2))/(1+(2*(omega_tau^(1-alpha))*
sin(alpha*pi/2))+(omega_tau^(2*(1-alpha))));

tan_delta_wetskin = eps_imag_wetskin/eps_real_wetskin;

% Muscle

eps_inf = 4;
eps_delta = 50;
tau_ps = 7.23;
tau = 7.23*(10^-12);
```

```
sigma = 0.2;
omega_tau = 2*pi*f*tau;
alpha = 0.1;

eps_muscle = eps_inf + (eps_delta / (1+(omega_tau^(1-
alpha))))+(sigma/(2*pi*f*epsilon_not));
eps_real_muscle = eps_inf + (eps_delta * (1+(omega_tau^(1-alpha)*
sin(alpha*pi/2))))/(1+(2*omega_tau^(1-alpha)*
sin(alpha*pi/2))+(omega_tau^(2*(1-alpha))))
eps_imag_muscle = (eps_delta*omega_tau^(1-
alpha)*cos(alpha*pi/2))/(1+(2*(omega_tau^(1-alpha))*
sin(alpha*pi/2))+(omega_tau^(2*(1-alpha))));

tan_delta_muscle = eps_imag_muscle/eps_real_muscle;


% Fat

eps_inf = 2.5;
eps_delta = 3;
tau_ps = 7.96;
tau = 7.96*(10^-12);
sigma = 0.01;
omega_tau = 2*pi*f*tau;
alpha = 0.2;

eps_fat = eps_inf + (eps_delta / (1+(omega_tau^(1-
alpha))))+(sigma/(2*pi*f*epsilon_not));
eps_real_fat = eps_inf + (eps_delta * (1+(omega_tau^(1-alpha)*
sin(alpha*pi/2))))/(1+(2*omega_tau^(1-alpha)*
sin(alpha*pi/2))+(omega_tau^(2*(1-alpha))))
eps_imag_fat = (eps_delta*omega_tau^(1-
alpha)*cos(alpha*pi/2))/(1+(2*(omega_tau^(1-alpha))*
sin(alpha*pi/2))+(omega_tau^(2*(1-alpha))));

tan_delta_fat = eps_imag_fat/eps_real_fat;

% Bone

eps_inf = 2.5;
eps_delta = 10;
tau_ps = 13.26;
tau = 13.26*(10^-12);
sigma = 0.02;
omega_tau = 2*pi*f*tau;
alpha = 0.2;

eps_bone = eps_inf + (eps_delta / (1+(omega_tau^(1-
alpha))))+(sigma/(2*pi*f*epsilon_not));
eps_real_bone = eps_inf + (eps_delta * (1+(omega_tau^(1-alpha)*
sin(alpha*pi/2))))/(1+(2*omega_tau^(1-alpha)*
sin(alpha*pi/2))+(omega_tau^(2*(1-alpha))))
eps_imag_bone = (eps_delta*omega_tau^(1-
alpha)*cos(alpha*pi/2))/(1+(2*(omega_tau^(1-alpha))*
sin(alpha*pi/2))+(omega_tau^(2*(1-alpha))));

tan_delta_bone = eps_imag_bone/eps_real_bone;
```